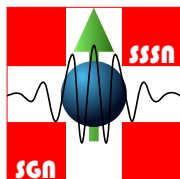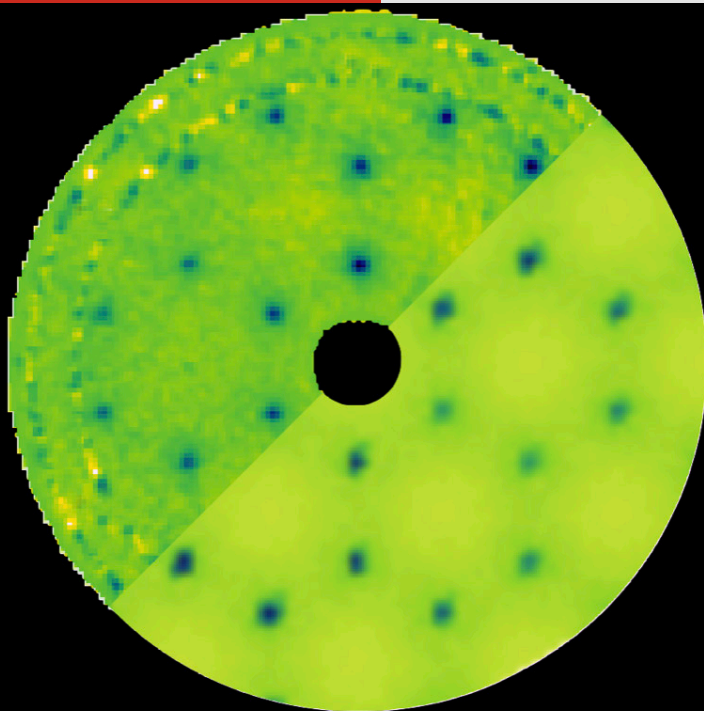# SWISS NEUTRON NEWS

Schweizerische Gesellschaft für Neutronenforschung
Société Suisse de la Science Neutronique
Swiss Neutron Science Society

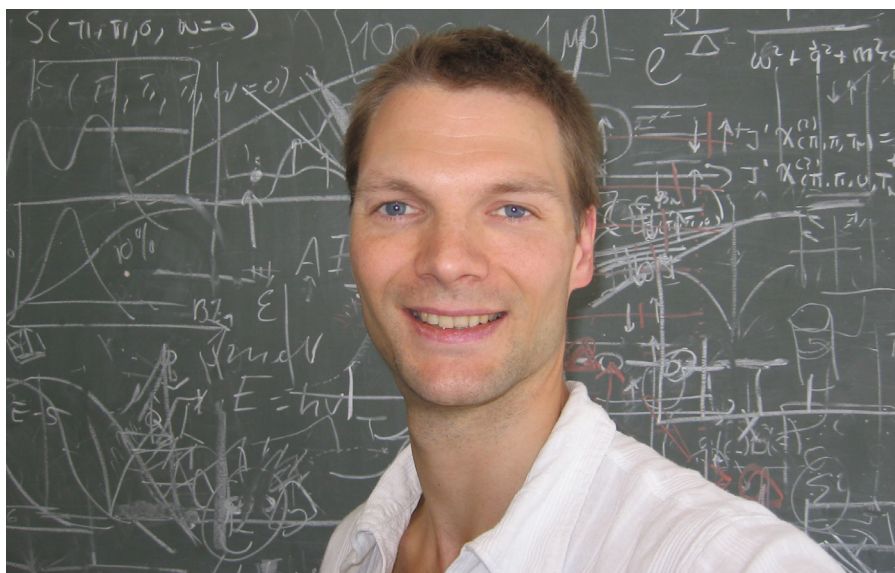# Contents

The President's Page

Dear fellow neutron scientists,

Welcome to this issue of Swiss Neutron News, where you can find 3 exciting artilces on respectively the performance after SINQ guide upgrades - which is a great achievement to the benefit of all us users, a beautiful piece of science observing plaquette fluctuations in $YbBr_3$, and high precision nuclear data on ^{53}Mn, which is an example of how wide the span of science at neutron sources is, and the reason our society's name was changed from Swiss Neutron Scattering Society to Swiss Neutron Science Society. I would like to thank the authors of these contributions and congratulate them on their achievements.

Another document that might interest you is the Swiss Neutron Science Roadmap [1], which was written as one of the thematic roadmaps intended to serve as basis for the 2023 edition of the Swiss Roadmap for Research Infrastructures [2].

Also here, I would like to thank the many colleagues who contributed to developing this roadmap vision and the entire user community for the many inputs and feedbacks we received in the process. As outlined in the findings, there are multiple exciting opportunities in the coming years, but also a few challenges that requires collaboration and action for us to continue to deliver the highest level of excellent science.

I wish you all a successful spring, an enjoyable summer and a productive autumn until we may hopefully meet in person at our next general assembly.

Henrik M. Rønnow

[1] https://scnat.ch/en/for_a_solid_science/networks_and_infrastructures/research_infrastructures/uuid/i/23635943-a35c-5447-a0a3-f8a5ba5d823b-Neutron_Science_Roadmap
[2] https://www.sbfi.admin.ch/sbfi/en/home/research-and-innovation/research-and-innovation-in-switzerland/swiss-roadmap-for-research-infrastructures.html

SINQ – Performance of the New Neutron Delivery System

Thomas Geue*, Fanni Juranyi, Christof Niedermayer, Joachim Kohlbrecher, Jochen Stahn, Urs Gasser, Masako Yamada, Christine Klauser, Michel Kenzelmann, Christian Rüegg, and Uwe Filges
Paul Scherrer Institute, Forschungsstrasse 111, 5232 Villigen PSI, Switzerland

* Corresponding author: thomas.geue@psi.ch, https://orcid.org/0000-0002-7932-5574

Abstract

The Swiss spallation neutron source SINQ at Paul Scherrer Institute (PSI) has been in operation since 1996 using an optical guide system to transport low-energy neutrons from the source to the neutron beam lines. Clear signs of degradation in the guide system motivated us to redesign all neutron guides, which were then replaced in 2019/2020. All instruments received new tailored guides and SINQ operation was resumed in July 2020. Neutron flux measurements before and after the upgrade show that the expected instrument-dependent flux gain of a factor 2 to 10 was achieved. Furthermore, the fast-neutron background in the guide hall could be suppressed with an improved shielding in the guide bunker. The upgrade was completed with a slight delay due to the corona pandemic and in full compliance with the financial budget.

The Swiss spallation neutron source SINQ at Paul Scherrer Institute (PSI) has been in continuous operation (eight months per year) since 1996. The neutron source was the first of its type and delivers a continuous neutron flux of 10^{14} n $cm^{-2}s^{-1}mA^{-1}$ [1]. In SINQ, the protons from the large particle accelerator HIPA [2] strike a lead target, leading to the generation of neutrons through spallation, which are available for experiments [3], see Fig.1. In addition to thermal neutrons, a moderator made of liquid deuterium (operated at 25 K) enables the production of cold neutrons, which have a lower energy spectrum. These neutrons have proved to be particularly valuable in materials research, condensed matter physics and in the investigation of biological systems. In the past years, the neutron flux has been boosted by increasing the proton current to the SINQ target from 850 µA to 1.8 mA.

SINQ was one of the first facilities to use at the time newly developed optical guide systems to transport cold neutrons (established in 1994). Metal-coated glass conduits (so called "supermirrors") guide neutrons over longer distances (roughly 15 to 70 m) by means of reflection with a low loss of intensity. The efficiency of these neutron guides has steadily increased with advances in manufacturing technology. The critical reflecting angle has been increased by a factor of 3-4, and the reflectivity at a given angle also increased. As the guide components at SINQ degraded considerably over time, in March 2017 PSI decided to carry out a comprehensive upgrade of the neutron guide system in 2019/2020. A small project group started in 2014 to prepare for the SINQ upgrade, and made the necessary calculations for different project options. The focus of the pre-study was on an upgrade of the neutron guides and of the liquid deuterium moderator. The idea was to optimize the instruments from the neutron source to the detector. The study has shown that a geometrical change of the moderator volume delivers roughly 20-50% more slow neutrons to the instruments. Due to the complexity of a moderator exchange, this project part was postponed for later realization.

The second part of the study was related to the guide geometries and their coatings. First evaluations showed that instruments, which can be operated with a divergent neutron beam can profit not only from the better supermirror coating, but also from the advanced guide geometry. When appropriate, these advanced geometries, allows for focus-

Figure 1
View into the SINQ guide hall after the upgrade (© J. Welte (PSI); March 2, 2021)

Guide number	Instrument	Guide length and type	Manufacturer
Monolith insert, sector 10 (RNR11–17)	All	4.5m (straight/elliptic)	S-DH, Mirrotron
RNR11	FOCUS	68m (ballistic/elliptic)	Swiss Neutronics, PSI
RNR12	DMC (Narziss, Orion)	45m (straight)	Swiss Neutronics
RNR13	Rita-II / CAMEA	31m (elliptic)	Swiss Neutronics
RNR14	TASP (Morpheus)	42m (straight)	Mirrotron
RNR15	SANS-LLB	50m (straight)	Mirrotron
RNR16	SANS-I	26m (straight)	Axilon, Swiss Neutronics, PSI
RNR17	AMOR	18m (Montel/elliptic)	Axilon, Swiss Neutronics, PSI

Table 1
Guide systems RNR11 to RNR17 after SINQ upgrade

ing of the neutron beam onto smaller samples. Sample size, which is directly linked to the signal amplitude, is often limited by sample availability, e.g. novel materials, and/or geometrical conditions from extreme condition sample environment. According to the calculations in the study, the neutron flux at the sample position could be increased up to one order of magnitude for the new guide geometries, compared to the conventional neutron guides.

The SINQ guide system consists of seven independent guides serving seven user and three in-house instruments, one more instrument will be added in 2022 (Laue camera FALCON). The guides are designated as RNR11 … RNR17 (see table 1).

The SINQ upgrade project started on March 1, 2017 with an overall budget of 17.1 MCHF (≈15.5MEur). More than 300m guide system (including new vacuum systems, new shielding concept, new shutter concept, new area access systems, water piping, power grid, computer network and control sensors) had to be replaced in the period from January 2019 to May 2020. Besides the complete exchange of all neutron guides the complete guide infrastructure was newly constructed and built. The removal of all guides was completed in mid-February 2019 after six weeks of demolition work. Then the prefabrication of additional shielding, supporting pillars and beam supports was started and the complete installation work was done in parallel.
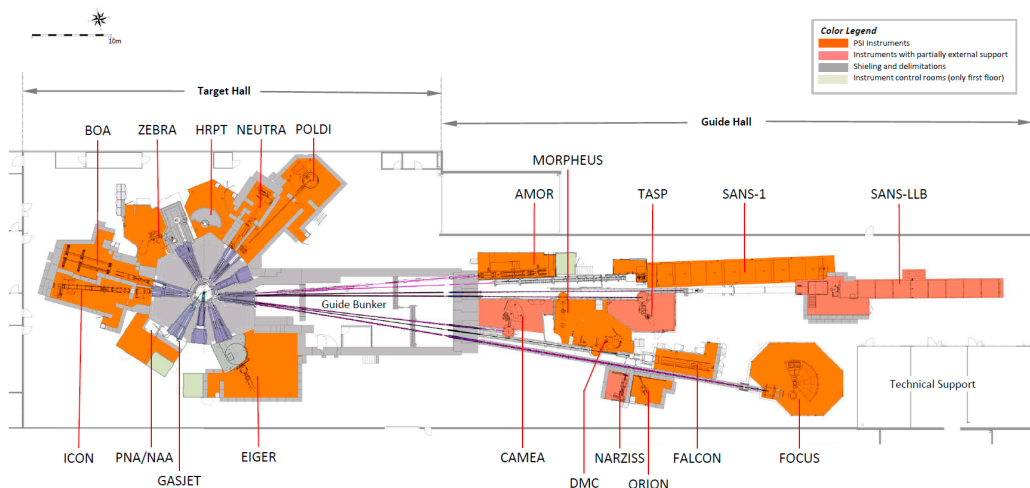
Figure 2

Gain factors in guides RNR11 to RNR17 at instrument position compared to 2018 (gold foil, fission chamber (instrument monitors) or reference sample measurements) * SANS LLB compared to the old SANS-II instrument; ** Gain factor includes also the new Ge monochromator at Orion.

In the remaining period in 2019 and the first 2.5 month in 2020, the new shielding and all seven neutron guides were constructed (Fig. 3), the last guide was finished on March 17, 2020, which was the first day of the Swiss corona pandemic lockdown. Most of the work was slowed down due to the pandemic, but the final delay of about 2 months was relatively small. Finally, the SINQ was switched on again on July 20, 2020. After commissioning of the neutron source and the attached instruments, user operation was resumed on August 4, 2020.

Gold foil, fission chamber (instrument monitors) and reference sample measurements yielded intensity gain factors between 2 and 10 (see Fig. 2), which agrees very well with the simulated predictions. All guides were simulated in McStas [4]. Furthermore, the improved shielding inside the bunker, especially a shielding wall composed of 0.5m borated polyethylene (PE) and 0.1m steel, reduced the neutron background in the experimental hall. MCNPX simulations predicted a factor 6 background suppression by the PE wall over a wide energy range, inside the bunker. We measured a background ratio of factor 10 at the two sides of the PE wall (12 and 30 m from the source) with a Bonner Sphere Spectrometer [5]. Outside the neutron guide bunker, no fast neutrons were detected along the guides of all instruments with a dose rate monitor. During the reference sample meas-
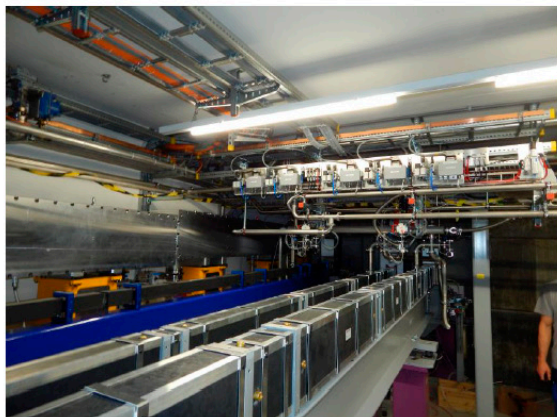
Figure 3
New guides installed in the pre-bunker (left) and the neutron bunker (right). A new shielding wall of borated polyethylene has been installed to reduce background levels (not shown here).

urements at AMOR no fast neutrons were observed in the detector too.

Besides the complete guide replacement, three user instruments receive major upgrades: The powder diffractometer DMC will be equipped with a highly efficient two-dimensional 3He detector and the novel multiplexing spectrometer CAMEA [6] replaces the Rita-II backend. The reflectometer AMOR was completely redesigned. The reflectometer is now equipped with a Selene-type guide [7], which is an advanced Montel neutron optics (2x9m optics segments with a variable neutron beam focusing down to 1x3mm^2 at the sample po-
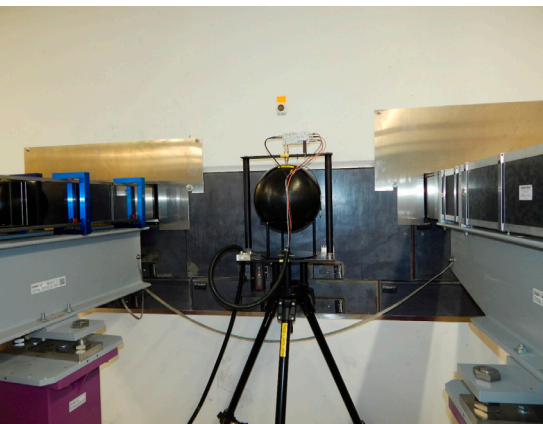

Figure 4
Neutron spectrum measurement with a Bonner Sphere Spectrometer system behind the mineral cast wall (12m from the source). The measured background was lower by a factor of 10-20 at the rear end of the bunker (30m from the source).
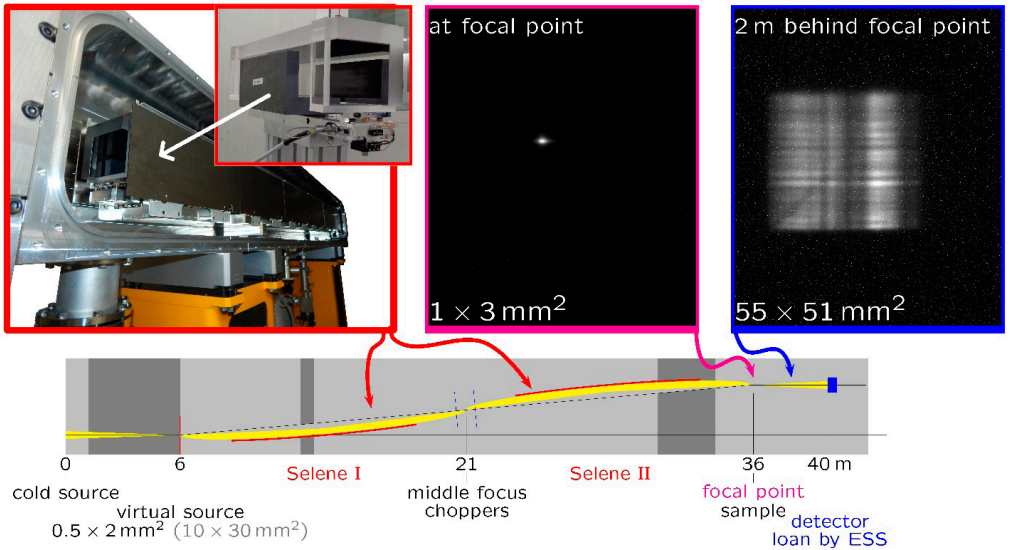
Figure 5

36 high precision optics components were put together to form the two halves of the Selene neutron guide. First beam tests on AMOR on August 21, 2020 proves successfully the focusing of the Montel optics.

sition, see Fig. 5) with an extrapolated neutron flux gain factor up to 30 for small samples.

To our best knowledge, this integrated high precision neutron optics setup is the first of its kind to be fully implemented for a neutron scattering instrument in the world. In the second half of 2020, first tests with the Montel optics at AMOR were carried out. Although the AMOR upgrade is not yet finished, one can extrapolate to future capabilities based on preliminary test measurements [8].

The focusing property was checked by using a scintillator and CCD camera at the focal position (the future sample position) and the minimum aperture size or 0.5x2 mm^2 at the initial focal point (virtual source), 30 m upstream (Fig. 5, bottom). The image of this aperture was 1x3 mm^2 (Fig. 5, top center), which is well within the specifications. The relevant gain factor for measurements was estimated by comparing counting times before and after the upgrade for a typical sample, where resolution, statistics and measurement range were about similar. For the present state without flight tubes and a detector covering of only 40% of the beam, a counting time reduction by one order of magnitude was obtained for a 10x10 mm^2 sample (Figure 5, right). With the fully equipped instrument, a total counting time reduction of 1/30 is ex-
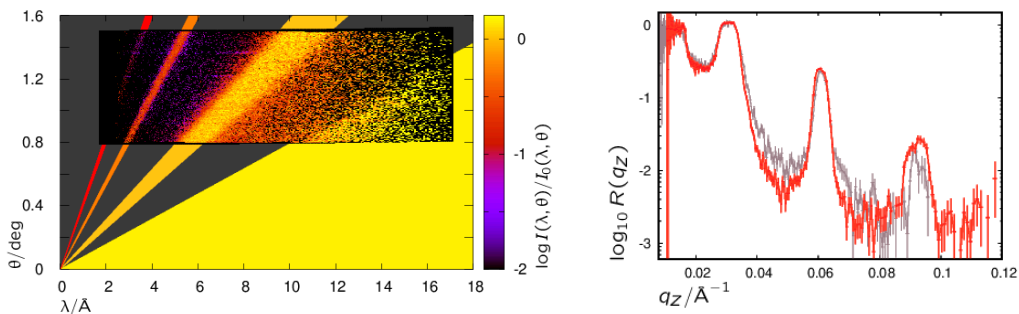
Figure 6

A reference sample (10x10 mm² NiTi supermirror) was measured with 1x3 mm² focusing. The counting time for comparable data quality (red curve) was a factor of 10 less compared to the reference measurement in 2018 (grey curve).

pected for samples, which are 8-20 mm broad, i.e. which can fully profit from the focused beam.

In the future, scientists will greatly benefit from the sharply increased flux, in particular for small hard condensed matter samples while soft matter and biology studies will profit from a lower gain factor of 2 to 5. In this case, full use of the focused beam is not possible due to incoherent scattering or a sample size larger than the beam spot.

Furthermore, the PA 20 SANS instrument was transferred from Laboratoire Léon Brillouin, Saclay France to PSI and will be installed until end of 2021. It will be taken into operation as SANS-LLB in April 2022.

In August 2020, a series of comparative measurements with reference samples was set up at the cold instruments to demonstrate the gain in flux for the new guide systems. First user experiments are very promising (see Fig. 7).

The SINQ upgrade at PSI and the improvements in the performance of the neutron guide systems as well as the research instruments was highly successful! With a delay of roughly 2 months only due to the corona pandemic lockdown and in full compliance with the financial budget, the SINQ upgrade is a success story. The entire project team is looking forward to a SINQ operation with increased performance at the benefit of the national and international scientific community.

«Instrument upgrade» box:

Time-of-flight spectrometer Focus: The intensity increase at the sample position is between 4 and 2 for the incoming wavelength range of 2-6Å ((002) reflection of the PG monochromator). After the upgrade, it possible to use the (004) reflection ($\lambda/2$) too. We could measure excitations up to 50 meV in a user experiment. The resolution and relative back-
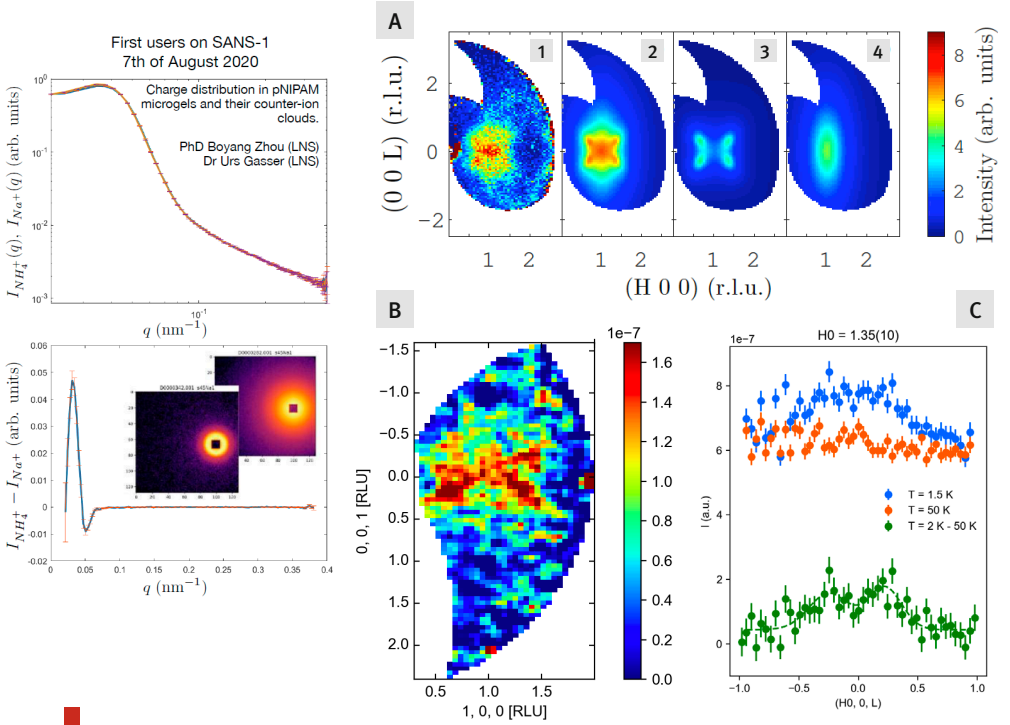
Figure 7

First results of measurements with reference samples after commissioning of the cold instruments in early August 2020; left: SANS measurements of the charge distribution in pNIPAM microgels and their counter-ion clouds (B. Zhou and U. Gasser, August 7, 2020); right: (A1) Competing quantum critical fluctuations measured at bench mark cold neutron chopper spectrometers, such as CNCS at the Spallation Neutron source in USA. (A2-3) Theoretical models. (B) Competing quantum critical fluctuations measured at CAMEA. (C) One-dimensional line cut along (1.35(10), 0, L). The data are consistent with the reported results from CNCS. (D. G. Mazzone).

ground remained unchanged. The new ballistic guide is described in detail elsewhere [9].

DMC Diffractometer: DMC will be equipped with a new, position sensitive detector and a new sample table. The expected flux gain on the detector is about a factor of 10. Hot commissioning is planned for September 2021.

Multiplexing TAS Spectrometer Rita II / CAMEA: The novel multiplexing backend CAMEA [6] was installed as a secondary instrument at RITA II in 2018. After the guide upgrade, few in-house measurements were performed in 2020, which demonstrated the large performance gain for overview studies

of low-energy dynamics (see Fig. 7). The installation of a large, doubly focusing monochromator in July 2021 will complete the upgrade of the instrument and facilitate the transport of the full neutron flux from the virtual source at the end of the guide to the sample.

TAS Spectrometer TASP: The flux at the sample position is increased by a factor of 2 due to the better supermirror coating and slight increase in guide cross section.

SANS I: In the shutdown 2021, the collimation was realigned. An additional gain of 20-30 % is expected. The guide upgrade resulted in a factor 2 higher neutron flux at the sample position.

Reflectometer AMOR: Commissioning is planned for 2022. Further details can be found in the main text.

The next SINQ Proposal Deadlines are May 15 and November 15, 2021. Users are encouraged to discuss their proposals with the instruments scientists in order to best profit from the improvements

Disclosure statement

The authors declare that they have no conflict of interest.

References

[1] www.psi.ch/en/sinq

[2] https://www.psi.ch/en/media/the-psi-proton-accelerator

[3] https://www.psi.ch/en/media/our-research/the-proton-accelerator-forty-years-of-top-flight-research

[4] mcstas.org, DOI: 10.3233/JNR-190108 (2019)

[5] B. Wiegel, A.V. Alevra, NIM A **476**/**1-2** (2002) 36-41

[6] https://www.psi.ch/en/sinq/camea/description; F. Groitl et al., Rev. Sci. Instr. **87/3** (2016) 035109; J. Lass et al., in preparation

[7] J. Stahn, A. Glavic, Nuclear Instruments and Methods A **821** (2016) 44-54

[8] G. Mauri et al., JINST **15** (2020) P03010

[9] F. Juranyi et al., will be submitted to the Special Issue "New Trends in Neutron Instrumentation" in Quantum Beam Science

Observation of plaquette fluctuations in the spin-1/2 honeycomb lattice YbBr$_3$

C. Wessler [1]*, **B. Roessli** [1], **K.W. Krämer** [2], **B. Delley** [1], **O. Waldmann** [3], **L. Keller** [1], **D. Cheptiakov** [1], **H.B. Braun** [2,4,5], **and M. Kenzelmann** [1],

[1] Laboratory for Neutron Scattering and Imaging, Paul Scherrer Institut, Villigen, Switzerland

[2] Department of Chemistry and Biochemistry, University of Bern, Bern, Switzerland

[3] Physikalisches Institut, Universität Freiburg, Freiburg, Germany

[4] Theoretical Physics, ETH Zürich, Switzerland

[5] Dublin Institute for Advanced Studies, Dublin 4, Ireland

* To whom correspondence should be addressed; E-mail: christian.wessler@psi.ch

Abstract

Quantum spin liquid materials are widely studied to improve our understanding of quantum entangled spin correlations in the absence of magnetic long-range order at T = 0 K. However, it is a challenging task to unambiguously identify a quantum spin liquid since it is difficult to measure quantum entanglement directly. Fortunately, neutron scattering is capable to measure fractionalized excitations that are a characteristic of quantum spin liquids. We studied YbBr$_3$ by neutron scattering whose magnetism is a realization of an effective S = 1/2 Heisenberg honeycomb lattice where nearest and next-nearest neighbor interactions compete. YbBr$_3$ avoids order down to at least T = 100 mK and features a dynamic spin-spin correlation function with broad continuum scattering typical of quantum spin liquids near a quantum critical point. The continuum in the spin spectrum is consistent with plaquette type fluctuations. Our study is the experimental demonstration that strong quantum fluctuations can exist on the honeycomb lattice even in the absence of Kitaev-type interactions, and opens a new perspective on quantum spin liquids.

Search for quantum spin liquids

Quantum spin liquids (QSL) do not show magnetic order even at absolute zero temperature and their distinguishing property is quantum long-range entanglement of its interacting magnetic moments. What attracts interest in QSLs is the prospective application of the long-range entanglement in quantum communications[2, 3] as well as possible realizations of fault-tolerant quantum computers that operate with anyon quasi-particles[2] which exist in a class of quantum spin liquids.[4, 5] Currently, a lot of research is done on QSL and promising candidate materials were proposed. However, there remains the challenging task to unambiguously identify a QSL in experiments. Inelastic neutron scattering (INS) provides the possibility to detect fractionalized excitations,[6] a distinguishing feature of QSL, which manifests as a broad continuum.

The basic ingredient for a QSL are strong quantum fluctuations that prevent the ordering of the magnetic ground-state. In general, lowering the dimension will increase quantum fluctuations. In one-dimension QSLs have been identified in antiferromagnetic (AF) spin chains. Case in point are $KCuF_3$[7] and $Cu(C_6D_5COO)_2\,3D_2O$.[8] In two- and three-dimensions, quantum fluctuations can be enhanced by frustration, and there are several routes to achieve this: The inherent geometrical frustration of kagome,[9] triangular,[10] spinel[11] and pyrochlore[12] lattices may prohibit long-range ordering at low temperatures. Another route is frustration by bond-dependent anisotropic interactions with the honeycomb lattice as the typical example. The honeycomb lattice received relatively little attention until Kitaev's

work[4] when it was shown that a new form of exactly solvable . Representatives materials are α-$RuCl_3$,[13] Li_2IrO_3[14] and $H_3LiIr_2O_6$[15] which show signatures of spin correlations due to quantum entanglement. Quantum fluctuations can also arise from the frustration between nearest and next-nearest neighbor exchange interactions. This is another possibility in the honeycomb lattice to have a QSL ground-state in particular since quantum fluctuations are already enhanced compared to the square lattice due to the lower number of neighboring spins. When next-nearest neighbor frustrating exchange interactions are sufficiently large compared to the nearest neighbour exchange, theories predict a quantum phase transition from a Néel ground state into a quantum entangled state. However, there is no consensus on the nature of this ground state: Theories predict either a QSL[16, 17] or a plaquette valence bond crystal (pVBC)[18–20] with different magnetic excitations which include spinons,[16] rotons[20] or plaquette fluctuations.[21]

We studied the static and dynamic properties of the trihalide two-dimensional (2D) compound $YbBr_3$ that forms a realization of the undistorted $S = 1/2$ honeycomb lattice with frustrated interactions. Short-range magnetic correlations between the Yb moments develop below $T \approx 3\,K$, but the correlation length is only of the order of the size of an elementary honeycomb plaquette at $T = 100$ mK, consistent with a QSL ground state. Despite this short correlation length, inelastic neutron measurements reveal well defined dispersive low energy magnetic excitations close to the Brillouin zone center. At high energies and at the zone boundary, we observe a continuum of excitations that we in-
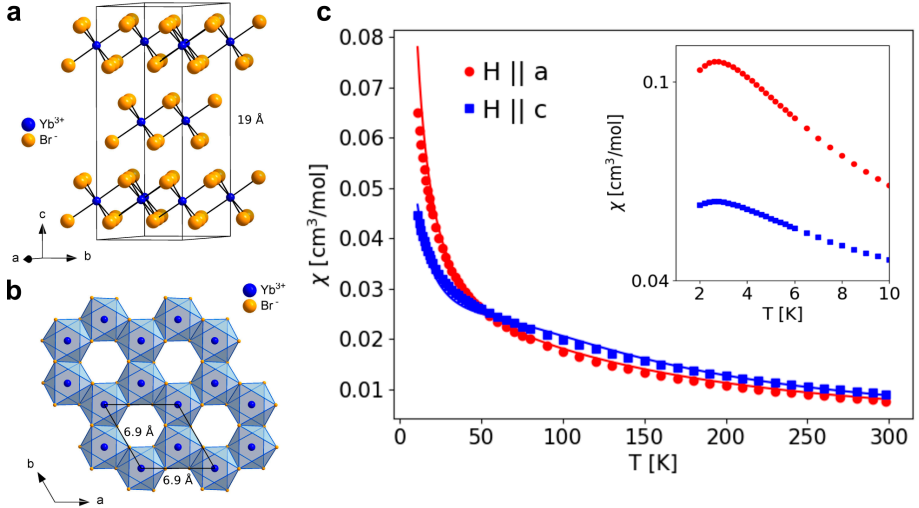
Figure 1
Magnetic susceptibility, crystal electric field and crystal structure. **a,** View along [210] on the unit cell of $YbBr_3$. **b,** Yb^{3+} honeycomb layer. **c,** Temperature dependence of the magnetic susceptibility χ of $YbBr_3$ for field orientations along the a- and c-axes. Solid lines are the calculated single-ion susceptibilities based on the crystal field (CEF)-parameters (Suppl.Info.). Inset: Measured low-temperature susceptibility showing a rounded peak around T = 2.75 K.

terpret as quantum fluctuations on an elementary hexagonal plaquette.

2D short-range magnetic order

$YbBr_3$ crystallizes with the BiI_3 layer structure in the rhombohedral space group $R\bar{3}$ (148), where the Yb ions form perfect two-dimensional (2D) honeycomb lattices perpendicular to the c-axis, as shown in Fig. 1. The temperature dependence of the magnetic susceptibility has a broad maximum around T = 3 K, but as shown below, there is no evidence for long-range magnetic order down to at least T = 100 mK. In the low temperature regime

below 10 K, we observe $\chi^{\perp} \approx 1.3\chi^{\parallel}$ which reflects a small easy-plane anisotropy in the plane perpendicular to the c-axis. The rare earth ion Yb^{3+} features a J = 7/2 ground-state multiplet that is split by the crystal-electric field (CEF), giving rise to a total of four Kramers doublets with the three excited CEF levels being observable via neutron scattering. The first excited level is observed at ~ 15 meV and the ground-state doublet is an effective S = 1/2 state. From an analysis of the measured susceptibility and the inelastic neutron data we obtain the CEF parameters (cf. Suppl. Info. of Ref. 1). They result in ground state expectation values of $\langle J_{\perp} \rangle = 1.2$ and $\langle J_{\parallel} \rangle = 0.8$

where the subscript indicates spin orientations measured relative to the c-axis in agreement with the observed easy-plane anisotropy from the magnetic susceptibility.

Fig. 2a shows the neutron diffraction pattern of the energy integrated magnetic scattering of YbBr$_3$ that was determined as the difference between diffraction patterns taken at T = 100 mK and T = 10 K in order to eliminate the contributions of nuclear scattering. No magnetic Bragg peaks are visible in the diffraction pattern, demonstrating that YbBr$_3$ avoids magnetic order down to at least this temperature. Diffuse magnetic scattering is centred at (1, 0, 0) and equivalent wave-vectors, which implies that the short-range cor-
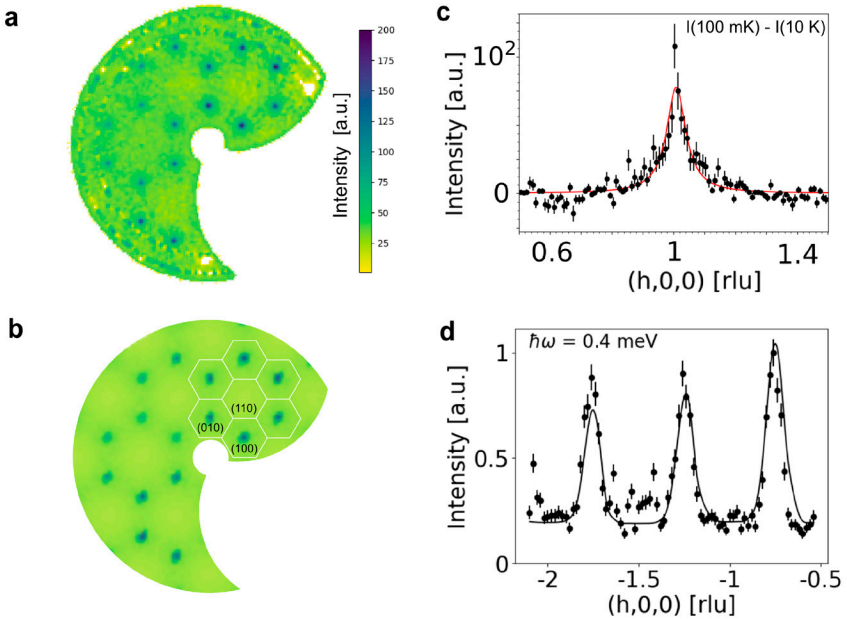
Figure 2

Magnetic diffuse scattering and correlation length. a, Magnetic diffuse scattering in YbBr$_3$ in the [h,k,0] plane at T = 100 mK, after subtraction of the nuclear Bragg contribution. **b,** Calculated magnetic diffuse scattering based on the spin-wave model including exchange and dipolar interactions. **c,** Cut through the diffuse scattering along the (h,0,0) direction. The line is a fit to the data with a Lorentzian function. [Note that the presence of paramagnetic scattering at 10 K leads to a negative background in the 100 mK data after subtraction]. **d,** Constant-energy scan for $\hbar\omega$ = 0.4 meV in YbBr$_3$ at T = 250 mK showing well-defined low energy excitations. The solid line represents the computed inelastic neutron scattering cross-section. Observed small peaks are due to spurious scattering and are not included in the model calculation.
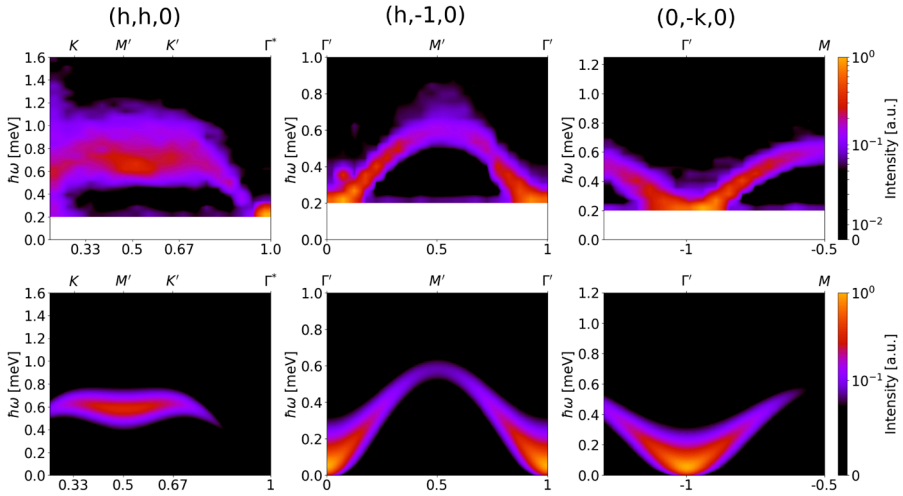
Figure 3

Magnetic excitations along high symmetry directions. False color plot of the observed (top) and calculated (bottom) inelastic neutron cross section of the magnetic excitations in YbBr$_3$ at T = 0.25 K. The intensity is shown on a logarithmic scale. Note the continuum of excitations around (1/2, 1/2, 0) and (1/2, −1, 0) which is not described by spin waves and is indicative of plaquette fluctuations.

relations are described by a propagation vector Q$_0$ = (0,0,0). Fig. 2b shows the diffuse scattering as calculated from the 2D spin wave theory described below, which reproduces both position and intensity of the observed diffuse scattering. Fig. 2c shows a cut along the Q = (q, 0, 0) direction which reveals diffuse scattering with Lorentzian line shape that reflects short-range magnetic order.[22] From a fit to the neutron intensity $I \propto \kappa^2/(q^2 + \kappa^2)$, we determine an in-plane correlation length between the Yb moments of $\xi = 1/\kappa \approx 10$ Å at T = 100 mK, comparable to the fourth nearest-neighbour distance of 10.66 Å which is ~1.25 times the

diameter of an Yb$_6$-hexagon plaquette.

A broad continuum atop sharp excitations

We measured well-defined magnetic excitations at T = 250 mK along three directions in the Brillouin plane. Within experimental resolution we observed a single excitation branch and no spin gap at the zone centre. As shown in the constant energy-scans in Fig. 2d and in Fig. 3, the magnetic excitations are sharp close to the Brillouin zone center. One of the key results of this study is the observation of a broadening of the spectrum when the disper-

sion approaches the zone boundary, as shown in Fig. 3. In fact, the inelastic neutron spectrum close to the zone boundary exhibits a continuum which extends to over twice the energy of the well-defined magnetic excitation. While low-lying excitations are sharp, these broad excitations are only observed at higher energies.

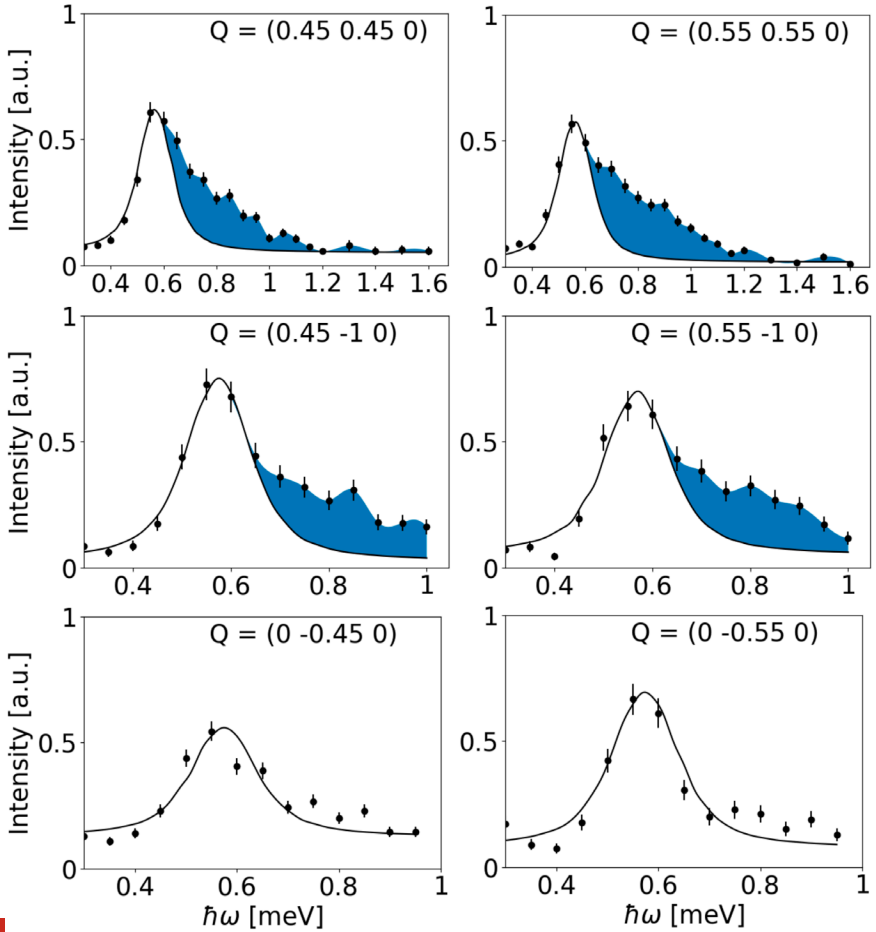While it may appear surprising that we observe well defined excitations even in the

Figure 4

Excitation continuum near the Brillouin zone boundary. Observed and simulated magnon spectra based on the spin-wave model explained in the text. The lines are fits to the data with a Lorentzian function. An intrinsic line-width of 0.1 meV was used for the simulation. The blue shaded areas indicate excitation continua.

presence of a correlation length of merely 10 Å, this agrees with the predictions of Schwinger-Boson[23] and modified spin-wave[24] theories which show that spin-waves can propagate in low-dimensional systems with shortrange Néel order. The well-defined excitations in YbBr$_3$ can be described by an effective S = 1/2 Hamiltonian including nearest and next-nearest neighbour Heisenberg exchange coupling, and dipolar interactions between the CEF ground state doublets,

$$H = -\frac{1}{2} \sum_{i,j} \sum_{\alpha,\beta} \mathcal{J}_{\alpha,\beta}(i,j) S_i^\alpha S_j^\beta, \quad (1)$$

where $\mathcal{J}_{\alpha,\beta}(i,j) = g_\alpha^2 \delta_{\alpha\beta} J(i,j) + g_\alpha g_\beta D_{\alpha,\beta}(i,j)$, with α, β = x, y, z cartesian coordinates of the hexagonal cell, and S_i^α is the α-component of a spin-1/2 operator at site i. Here $J(i,j)$, are the exchange coupling constants between distinct sites i and j, while $D(i,j)$ denote the dipolar interactions. For the calculation of the spin wave dispersion, we use the random phase approximation (RPA) around the Néel state with spins in the hexagonal plane and S = 1/2. Our measurements allow the determination of the exchange couplings, while the dipolar coupling is fixed by the magnetic moment. As shown in Fig. 3, we find good agreement between measured and calculated spin-wave dispersions. The nearest- and next-nearest-neighbour exchange interactions J$_1$, J$_2$ are obtained from a least-square fit to the data. We obtained g^{2}J$_1$ = 0.69(8) meV and g^{2}J$_2$ = 0.09(2) meV (see Suppl. Info. of Ref. 1 for details). We note that our spin wave theory does not describe all aspects of our experimental results: It predicts an optical branch for values of the easy-plane anisotropy that corresponds to the measured susceptibility (cf. Fig. 1), while we do not find experimental

evidence for such a second branch. Also it does not explain the existence of an excitation continuum as we shall discuss next.

As shown in Fig. 3, the magnetic excitation spectrum also features weaker broad scattering at energies where the optical branch is expected. This is particularly evident near the M-points at (0.5, 0.5, 0) and (0.5, 1, 0), where the excitations extend to 0.8 - 1 meV and are reminiscent of scattering observed in other low-dimensional antiferromagnets.[25, 26] In most materials, spin-waves are long-lived excitations that are resolution-limited as a function of energy. When the spin-waves are damped or interact with other spin-waves they have a finite life-time and the line-shape of the dynamical structure factor S(Q, ω) broadens. We have simulated the line-shape of S(Q, ω) derived from our model and convoluted it with the resolution of the spectrometer obtained from the Takin software[27] (cf. Methods Ref. 1). While the spin-wave model adequately explains the dispersion and intensity distribution close to the Brillouin zone centers, it does not reproduce the inelastic neutron line-shape close to the maximum of the dispersion of the spin-wave branch as shown in Fig. 4.

Competition between dipolar interactions and easyplane anisotropy

In YbBr$_3$ the Yb-ion has a large magnetic moment of the order of 2 μB and therefore the dipolar interactions cannot be neglected. At the classical level, one can show that they favour antiferromagnetic Néel order with the spins along the c-axis[28] enabled by a spin gap at the zone center of ~ 200 μeV. This spin gap caused by the dipolar interaction is reduced

by the CEF easyplane anisotropy which contributes to a destabilization of the Néel state at finite temperature (Supplement Fig. S2 of Ref. 1). At $g_{\mathrm{crit}} \approx g_{zz}/g_{xx} \equiv 0.985$ the spin gap closes and quantum fluctuations will be enhanced. Below that value the spins rotate into the basal plane. Linear spin wave theory predicts that easyplane anisotropy entails a lifting of the degeneracy of the two spinwave branches at the zone centre, and the splitting increases with increasing anisotropy. A large anisotropy in YbBr$_3$ would then become measurable since the branch separation becomes large enough to be resolved. A computation of S(Q, ω) at g$_{crit}$ is shown in Fig. 3 and describes the observed dispersion and intensities of the sharp excitations very well.

Experimentally, we have observed neither a splitting of spin waves nor a spin gap within the available energy resolution. This suggests that the absence of the long-range order in YbBr$_3$ at T = 100 mK is caused by the competition between easy-plane anisotropy and dipolar interactions that accentuates quantum fluctuations. This places YbBr$_3$ close to the quantum critical point towards a QSL of the spin-1/2 Heisenberg Hamiltonian on the honeycomb lattice.

It's in the plaquette

Our experiment provides clear evidence for the presence of a continuum of excitations at high energies in YbBr$_3$. We can exclude the possibility of the line-shape broadening being caused by two-magnon decay. The necessary cubic anharmonicities for strong two-magnon scattering are absent for collinear magnets such as YbBr$_3$.[29] We observe that the intensity of the continuum is stronger at the M' points along (h,-1,0) and (h,h,0) directions whereas it is absent along (0,k,0) and at the Γ and Γ* points.

We found that this modulation of the neutron intensity associated with the continuum can be reproduced by a random-phase approximation (RPA) calculation for a hexamer plaquette with the exchange parameters obtained from the spin-wave calculations (cf. Methods of Ref. 1). This picture of local excitations in YbBr$_3$ is supported by an analogous calculation of the magnetic susceptibility which shows a broad maximum at $\mathrm{T} \simeq 4 \ \mathrm{K}$ (see Supplement of Ref. 1). Similar excitations associated with small spin clusters were also observed in the spinel lattice.[30] Our neutron measurements are also in agreement with recent Monte-Carlo calculations of the dynamical structure factor for the frustrated honeycomb lattice[20] that show a deconfined two-spinon continuum[31] with enhanced intensity at the zone boundary due to proximity of a quantum critical point.

Summary

In summary, we have shown that the magnetic ground-state of YbBr$_3$ exhibits only short range order well below the maximum in the static susceptibility. Analysis of the dispersion of the magnetic excitations reveals competition between the nearest-neighbour and next-nearest-neighbour exchange interactions, but no mode softening. We observed a continuum of excitations with the spectrum of excitations extending to approximately twice the energy of the position of the maximum in S(Q, ω). The neutron inelastic intensity due to the continuum follows the modulation expected for the

fluctuations of a honeycomb spin plaquette. Our results demonstrate that YbBr$_3$ is a two-dimensional S = 1/2 system on the honeycomb lattice with spin-liquid properties without Kitaev-type interactions. The observation of the continuum associated with localized pla-quette excitations supports the view of a de-confined quantum critical point[32] in the frus-trated honeycomb lattice, in agreement with results from coupled cluster methods, density matrix renormalization group calculations and Monte-Carlo simulations.[19, 20, 33]

REFERENCES

1. Wessler, C. et al. Observation of plaquette fluctuations in the spin-1/2 honeycomb lattice. *npj Quantum Materials* **5**, 85 (2020).
2. Kitaev, A.Y. Fault-tolerant quantum computation by anyons. *Ann. Phys.* **303**, 2-30 (2003).
3. Nayak, C., Simon, S.H., Stern, A., Freedman, M., & Das Sarma, S. Non-Abelian anyons and topological quantum computation. *Rev. Mod. Phys.* **80**, 1083 - 1159 (2008).
4. Kitaev, A.Y. Anyons in an exactly solved model and beyond. *Ann. Phys.* **321**, 2-111 (2006).
5. Savary, L. & Balents, L. Quantum spin liquids: a review. *Rep. Prog. Phys.* **80**, 016502-016568 (2016).
6. Lacroix, C., Mendels, P. & Mila, F. Introduction to frustrated magnetism. *Springer series in solid-state science*, Springer (2011).
7. Tennant, D.A., Perring, T.G., Cowley, R.A. & Nagler, S.E. Unbound Spinons in the S = 1/2 Antiferromagnetic Chain KCuF$_3$. *Phys. Rev. Lett.* **70**, 4003-4006 (1993).
8. Dender, D.C., Hammar, P.R., Reich, D.H., Broholm, C. & Aeppli, G. Direct Observation of Field-Induced Incommensurate Fluctuations in a One-Dimensional S = 1/2 Antiferromagnet. *Phys. Rev. Lett.* **79**, 1750-1753 (1997).
9. Mendels, P.& Bert, F. Quantum kagome frustrated antiferromagnets: One route to quantum spin liquids. *C. R. Physique* **17**, 455-470 (2016).
10. Shimizu, Y., Miyagawa, K., Kanoda, K., Maesato, M. & Saito, G. Spin Liquid State in an Organic Mott Insulator with a Triangular Lattice. *Phys. Rev. Lett.* **91**, 107001 (2003).
11. Villain, J. Insulating Spin Glasses. *Z. Physik B* **33**, 31-42 (1979).
12. B. Canals & C. Lacroix, Pyrochlore Antiferromagnet: A Three-Dimensional Spin Liquid. *Phys. Rev. Lett.* **80**, 2933-2936 (1998).
13. Banerjee, A. *et al.* Proximate Kitaev quantum spin liquid behaviour in a honeycomb magnet. *Nature Materials* **15**, 733-741 (2016).
14. Singh, Y. et al. Relevance of the Heisenberg-Kitaev Model for the Honeycomb Lattice Iridates A$_3$IrO$_3$. *Phys. Rev. Lett.* **108**, 127203 (2012).
15. Kitagawa, K. *et al.* A spin−orbital-entangled quantum liquid on a honeycomb lattice. *Nature* **554**, 341-345 (2018).
16. Merino, J. & Ralko, A. Role of quantum fluctuations on spin liquids and ordered phases in the Heisenberg model on the honeycomb lattice. *Phys. Rev. B* **97**, 205112 (2018).
17. Wang, F. Schwinger boson mean field theories of spin liquid states on a honeycomb lattice: Projective symmetry group analysis and critical field theory. *Phys. Rev. B.* **82**, 024419 (2010).
18. Albuquerque, A.F. *et al.* Phase diagram of a frustrated quantum antiferromagnet on the honeycomb lattice: Magnetic order versus valence-bond crystal formation. *Phys. Rev. B* **84**, 024406 (2011).
19. Ganesh, R., van den Brink, J. & Nishimoto, S. Deconfined Criticality in the Frustrated Heisenberg Hamiltonian Honeycomb Antiferromagnet. *Phys. Rev. Lett.* **110**, 127203 (2013).
20. Ferrari, F. & Becca, F. Dynamical properties of Néel and valence-bond phases in the J$_1$ − J$_2$ model on the honeycomb lattice. arXiv:1912.09310 (2019).

21. Ganesh R., Nishimoto S., & van den Brink J. Plaquette resonating valence bond state in a frustrated honeycomb antiferromagnet, *Phys. Rev. B* **87**, 054413 (2013).

22. Collins, M.R. *Magnetic Critical Scattering* (Oxford University Press, 1989).

23. Mattsson, A., Fröjdh, P. & Einarsson, T. Frustrated honeycomb Heisenberg antiferromagnet: A Schwinger-boson approach. *Phys. Rev. B* **49**, 3997-4002 (1994).

24. Ghorbani, E., Shahbazi, F. & Mosadeq, H. Quantum phase diagram of distorted J_1-J_2 Heisenberg S = 1/2 antiferromagnet in honeycomb lattice: a modified spin wave study. *J. Phys.: Cond. Mat.* **28**, 406001 (2016).

25. Mourigal, M. et al. Fractional spinon excitations in the quantum Heisenberg antiferromagnetic chain. *Nat. Phys.* **9**, 435-441 (2013).

26. Han, T.-H. et al. Fractionalized excitations in the spin-liquid state of a kagome-lattice antiferromagnet. *Nature* **492**, 406-410 (2012).

27. Weber, T., Georgii, R. & Böni, P. Takin: An open-source software for experiment planning, visualization, and data analysis. *SoftwareX* **5**, 121-126 (2016).

28. Pich, C. & Schwabl, F. Order of two-dimensional isotropic dipolar antiferromagnets. *Phys. Rev. B* **47**, 7957-7960 (1993).

29. Zhitomirsky, M.E. & Chernyshev, A.L. Colloquium: Spontaneous magnon decays. *Rev. Mod. Phys.* **85**, 219-243 (2013).

30. Lee, S.-H. *et al*. Emergent excitations in a geometrically frustrated magnet. *Nature* **418**, 856-858 (2002).

31. Ferrari, F. & Becca, F. Spectral signatures of fractionalization in the frustrated Heisenberg model on the square lattice. *Phys. Rev. B*. **98**, 100405 (2018).

32. Senthil, T., Balents, L., Sachdev, S., Vishwanath, A. & Fisher, M.P.A. Quantum criticality beyond the Landau-Ginzburg-Wilson paradigm. *Phys. Rev. B*. **70**, 144407 (2004).

33. Bishop, R.F., Li, P.H.Y. & Campbell, C.E. Valence-bond crystalline order in the S = 1/2J_1 − J_2 model on the honeycomb lattice. *J. Phys.: Condens. Matter* **25**, 306002 (2013).

High precision nuclear data of ^{53}Mn for astrophysics and geosciences

J. Ulrich[1], R. Dressler[1]*, D. Schumann[1], P. Sprung[2]

[1] Laboratory of Radiochemistry (LRC), Paul Scherrer Institute, 5232 Villigen-PSI, Switzerland

[2] Hot Laboratory Department (AHL), Paul Scherrer Institute, 5232 Villigen-PSI, Switzerland

Correspondence: rugard.dressler@psi.ch; Tel: +41 (0) 56 310 24 69

1. Introduction

^{53}Mn ($t_{1/2} \approx 3.7$ Ma) is a short-lived cosmogenic radionuclide (SLR) mainly produced in free-zout phases of nuclear statistical equilibria of explosive burning in both thermonuclear and core-collapse supernovae explosions[1,2]. Although similar, supernova-produced radio-nuclides, e.g., ^{44}Ti or ^{60}Fe, can be observed directly at their astrophysical site of origin (see Fig. 1), this is unfortunately not the case for ^{53}Mn due to its low-energy radiation. Nevertheless, ^{53}Mn more recent astrophysical sources is detected in galactic cosmic rays by spacebased equipment on Earth's orbit[3] or in form of »cosmic fallout« of condensed interstellar material in sediments on Earth's surface. In 2019, supernovae-produced SLRs ^{60}Fe and ^{53}Mn were found in the Antarctic ice and their origin traced to the Local Interstellar Cloud, a dust cloudlet currently being traversed by Earth[4]. Such accreted interstellar dust can help to identify and date past supernovae events which occurred in the astronomical neighborhood[5,6,7].

It is assumed that the collapse of the protosolar nebula, marking the start of the evolution of our Solar system, was triggered by the ignition of a nearby supernova. As an additional consequence, large amounts of
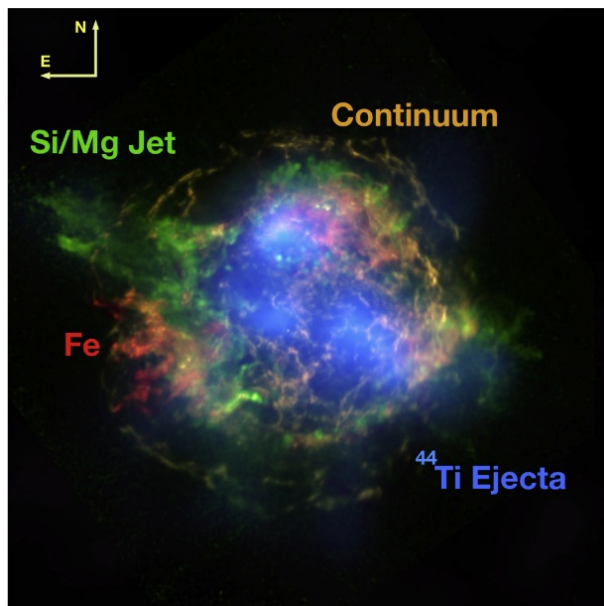
SLRs would have been injected into the newborn Solar system by this event. Analysis of meteoritic material from the early Solar system indeed confirmed the existence of SLRs including ^{53}Mn in the protosolar nebula. Although the primordial ^{53}Mn is now extinct, the former presence of ^{53}Mn can be detected by enhancements of its stable daughter ^{53}Cr, which are clearly observable in meteoritic inclusions originating from the early Solar system. Due to the half-life of ^{53}Mn of about 4 Ma, the ^{53}Mn/^{53}Cr chronometer can be used for precise dating of events in the early Solar System on the timescale of 20 Ma[9]. The amounts of initially present ^{53}Mn exceed what is provided by the stationary galactic chemical evolution. Thus, other scenarios, e.g., »pollution« of the presolar material by stellar winds from nearby Asymptotic Giant Branch (AGB) or Wolf-Rayet (WR) stars are discussed as alternative sources of these SLR enhancements in the early Solar system, but none of the postulated theories has been proven to be conclusive yet (see article[10] and references therein). The observed SLRs' abundancy patterns in the early Solar system, with ^{53}Mn being one of the key markers, can be used to reconstruct the course of events ultimatively leading to the formation of our Solar system. However, detailed knowledge of the production of SLRs in the respective astrophysical scenarios, their transport as well as destruction pathways is required. This translates on the microscopical level to the need for high precision nuclear data, in particular the cross-sections of all involved nuclear reactions and precise half-life values of the initial isotopes as well as the intermediate and end products, most of them being radioactive. The respective data are either used directly as an

input for corresponding stellar and nucleosynthesis models or, in combination with observed data, for benchmarking of the predictions and constraining the model parameters.

Besides [53]Mn of extrasolar origin, small amounts of [53]Mn are produced by the bombardment of surface-near rocks with high energy cosmic rays on Earth[11] and Moon[12] as well as in meteoritic material. The utilization of terrestrial spallogenic [53]Mn for exposure dating and reconstruction of landform processes has been successfully shown[11]. The interest in [53]Mn has been rising in the last years as the development of accelerator mass spectrometry (AMS) allowed reliable detection of ultra-low concentrations of [53]Mn in terrestrial materials with quantification abilities reaching values as low as [53]Mn/[55]Mn < 10^{-14} as described in[13]. As an example to illustrate the capabilities of contemporary state-of-the-art AMS, detection of only 12 atoms [53]Mn in 500 kg ice was reported in 2019[4]. But for any dating application involving [53]Mn, a precise value of the [53]Mn half-life is a mandatory requirement.

2. [53]Mn sources at PSI and the ERAWAST project

PSI operates several accelerator facilities and particle sources including a 590 MeV proton cyclotron with the world-wide highest thermal power, corresponding to a proton current of more than 2 mA. By interaction of the high energy, high intensity primary or secondary particles with various samples, targets, structural or shielding materials, a number of radioisotopes produced in unique amounts. This activation is usually considered as a negative side effect and the materials are disposed as radioactive waste. The ERAWAST

Figure 2
Disassembled copper beam dump[25] of the pion cancer therapy station. The beam dump had a length of 37 cm and a diameter of 8 cm. It was sawed into 3 cm to 9 cm long pieces to test the lateral and radial distribution of the exotic radionuclides (left). Later, 500 g of copper chips were drilled out of the central part with the beam entry point. These copper chips were used for radiochemical separation of [26]Al, [44]Ti, [53]Mn, [59]Ni and [60]Fe (right).
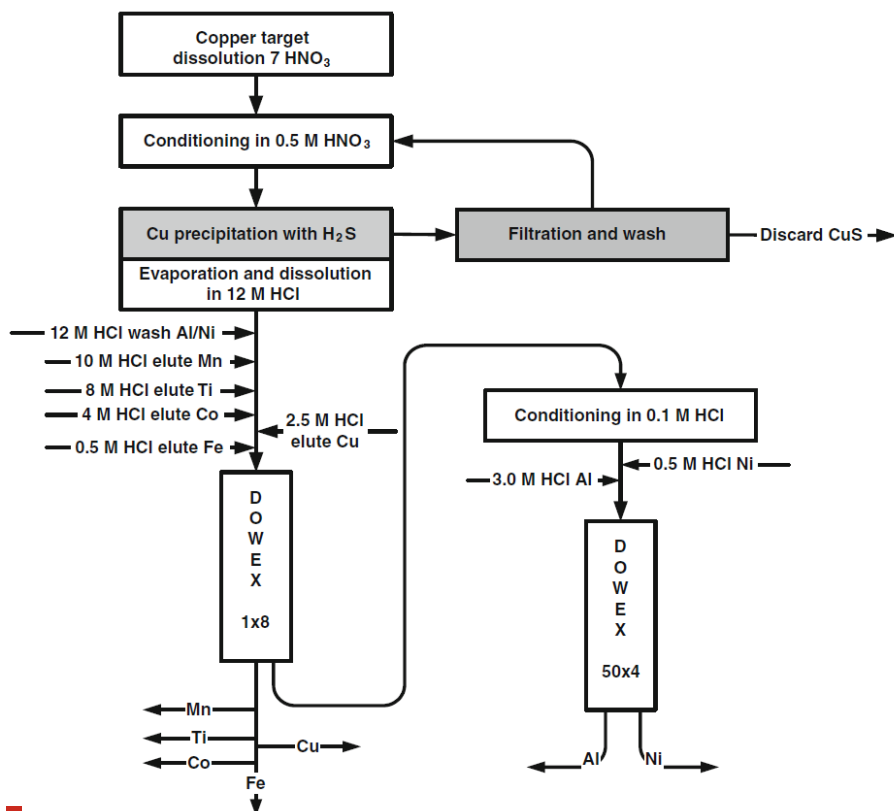
Figure 3
The radiochemical procedure used to extract [53]Mn (and other exotic radionuclides) from the samples of the copper beam dump material[26].

initiative (Exotic Radionuclides from Accelerator Waste for Science and Technology)[14] was started at PSI in 2006 with the aim to extract and purify these rare and exotic radioisotopes available at PSI in world-wide unique amounts using tailored radiochemical separation methods. Several radioisotopes, which are of large significance to astrophysics, geosciences or fundamental nuclear physics, were extracted in µg to mg amounts and made available to the scientific community for various high-profile experiments, among others [7]Be[15,16,17,18], [10]Be[19], [26]Al, [44]Ti[20,21] or [60]Fe[22,23,24].

The primary source of [53]Mn material used for the experiments described in this work was a copper beam dump of a pion cancer therapy station. The station (s. Fig. 2) was operated between 1980 and 1992 at PSI West areal. During this period, a total dose of about 0.16 Ah corresponding to 3.6×10^{21} protons of

590 MeV was accumulated on the beam dump, leading to a production of a broad spectrum of activation products. Following a 12 years long cooldown after decommissioning of the station, several drill samples were obtained in order to perform a radiochemical analysis of the activation products and their spatial distribution within the beam dump[25]. These drill cores were found to be a very promising source of multiple rare radioisotopes of particular interest for astrophysics – ^{26}Al, ^{44}Ti, ^{53}Mn and ^{60}Fe. A radiochemical separation procedure based on cation and anion exchange chromatography was developed in order to extract these radionuclides from the copper material with a high recovery (see Fig. 3). Additional radiochemical purifications were performed during the course of this work in order to remove radiochemical impurities still present in detectable amounts in the ^{53}Mn fraction extracted during ERAWAST.

About 7×10^{18} atoms ^{53}Mn (corresponding to about 40 kBq or 60 μg) were recovered. This stock is about a factor of ~10'000 higher than the amounts of ^{53}Mn used for any previous experiments aiming at the determination of the half-life or the neutron capture cross-section which had to rely on meteoritic sources or low-level activated materials. Furthermore, last such measurements were performed in the early 1970s and are still used as a reference despite their high uncertainties on a 10-15 % level which is inacceptable for most applications. The uniquely large ^{53}Mn amounts available at PSI and the overall progress in radioanalytical and mass spectrometric methods present an unique opportunity for a new determination of the neutron capture cross-section and the half-life of ^{53}Mn with drastically reduced uncertainties and enabling also cross-section measurements at a much wider range of neutron energies.

3. Neutron capture cross-section measurements

Only the thermal neutron capture cross-section of ^{53}Mn was measured experimentally before the start of the work presented here. Considering the limited quantities of ^{53}Mn available in the past and the generally high thermal neutron capture cross-sections, an activation in a nuclear reactor posed the only viable option for such a measurement. A reference value of 70±10 barn is typically given in data compilations such as that of Mughabghab[27]. This value was obtained by averaging the results of three original measurements performed in the 1960s and 1970s[28,29,30] and its uncertainty of 15 % is unacceptably high according to modern standards. Before the advent of AMS, the preferred method of ^{53}Mn quantification was neutron activation analysis (NAA) using nuclear reactors[11] and for the majority of ^{53}Mn samples, NAA still remains the faster and more convenient analysis method as of today, despite the diminishing number of operating research reactors. Since a fundamental requirement for NAA is the precise value of the neutron capture cross section, a reduction of its uncertainty is directly transformed into an improvement in the accuracy of the NAA results.

The goal of this work is not just to remeasure the thermal neutron capture cross-section using higher material amounts and state-of-the-art methods in order to reduce its current uncertainty, but to investigate the feasibility of cross-section measurements at different neutron energies which were impos-
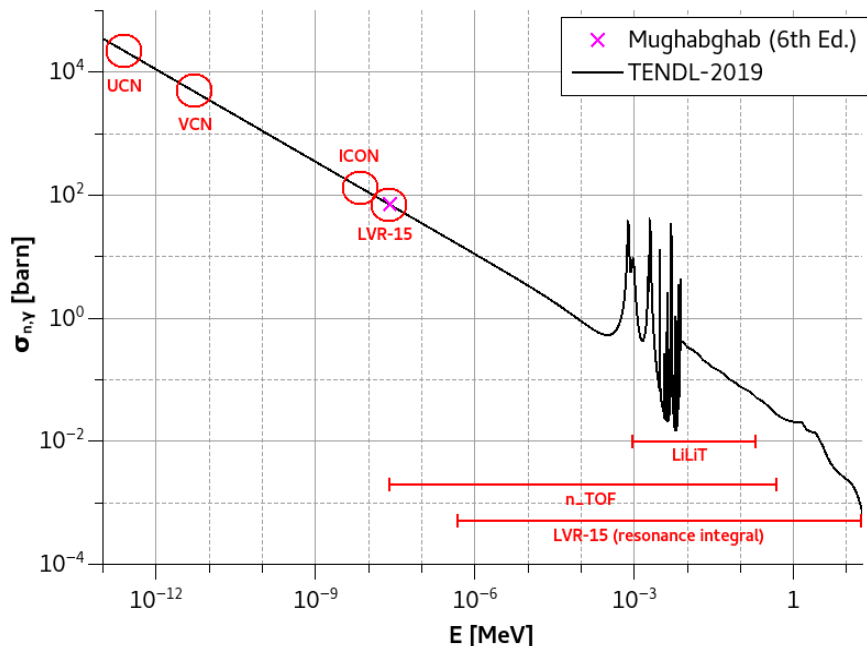
Figure 4

Thermal neutron capture cross-section of ^{53}Mn given in the current edition of Mughabghab's Atlas of Neutron Resonances[27] as 70±10 barn (purple), based on measurements from the 1960s and 1970s. This is currently the only energy for which experimental data is available. The theoretical predictions of the ^{53}Mn cross-section shape from the current version of the TENDL nuclear data library[31,32] is presented in black. Energy regions of the individual measurements performed in this work, covering virtually the whole energy range from 100 neV to several MeV, are marked in red.

sible in the past. We follow a highly ambitious experiment plan in order to measure the neutron capture cross-section of ^{53}Mn in different energy regions from ultra-cold neutron (UCN) energies of few hundreds neV up to fast neutrons of few hundreds keV, spanning twelve orders of magnitude of incident neutron energy (see Fig. 4). Whereas the measurements with cold and ultra-cold neutrons could be performed using PSI's own facilities, other experiments had to be realized with international collaboration partners from other high-grade research institutions. Cross-section measurement with very cold neutrons (VCN) was conducted at the PF2 beamline at ILL Grenoble (France), reactor irradiation at the LVR-15 research reactor at ÚJV Řež (Czech Republic) and activation with stellar-energy neutrons using the LiLiT facility at SARAF (Israel). Besides these activation experiments,

the possibility to scan the resonances in the [53]Mn excitation function using the time-of-flight (TOF) technique was investigated at the n_TOF facility at CERN. Unfortunately, the rather weak resonance structure of [53]Mn and the still limited amount of material yielded no usable signal. Similarly, although a method for cross-section measurements by the activation method with UCNs could be established and validated during the course of this work, the required amounts of [53]Mn would be too high to make such measurement feasible. In the following text, the details of the measurements of the thermal capture cross-section and the cross-section at stellar neutron energies will be given.

3.1 Thermal neutron cross-section determination

The thermal neutron capture cross-section was measured by the activation method with cold and reactor neutrons. The purified [53]Mn chloride solution was spiked with natural cobalt chloride in order to act as a neutron fluence monitor, utilizing the reaction [59]Co(n,γ) with well-known cross-section at thermal neutron energies. Three individual samples of about 3×10^{17} atoms [53]Mn each were prepared by dropping this solution on a $\varnothing = 0.6$ cm glass wool filter disc, fixed on transparent adhesive tape. After drying, the samples were sealed by a second layers of transparent adhesive tape, forming a disc of 2.6 cm diameter with the filter in the center. Left panel of Fig. 5 shows one of the finished samples. The exact amounts of the stock solution deposited on each target were traced gravimetrically. The stock solution was then analyzed by inductively coupled plasma mass spectrometry (ICP-MS) with respect to its [53]Mn and [59]Co concentration in order to obtain precise [53]Mn and [59]Co contents in each sample. Gravimetric standard adition with an extra addition of Fe as an internal standard[33,34] and reverse isotope dilution[35] were employed for this determinations. The analysis was performed on the Nu Instruments Plasma 3, multi-collector ICP-MS at the PSI Hotlab Facility using mass resolution settings sufficiently high to resolve molecular interferences comprising the plasma gas Ar. Instrumental mass discrimination was characterized and corrected for using analyses of a mixed Fe-Cr solution that was measured before and after sample analyses. Signal baselines include realistic signal contribution from the sample introduction system. These baselines were obtained under identical conditions and interspersing sample and standard analyses and represent signals recorded with the same pure acid (HNO_3) that was used in the sample and standard dilutions at equivalent concentrations. To correct for the isobaric interference of [53]Cr on mass 53, an aliquote of the analyte solution was taken, chromium was separated from manganese by anion exchange chromatography using the method described in[36] and the $^{52}Cr/^{53}Cr$ ratio of the manganese-free fraction was measured.

The activation experiment with cold neutrons was carried out at the ICON beamline[37] at the PSI's spallation neutron source SINQ with mean neutron energy of 8.53 meV. The samples were irradiated for twelve days in total, parallel to imaging experiments running at the beamline at the same time. A dedicated aluminum sample holder was designed in order to mount the samples directly behind the beam shutter and let the beam pass un-
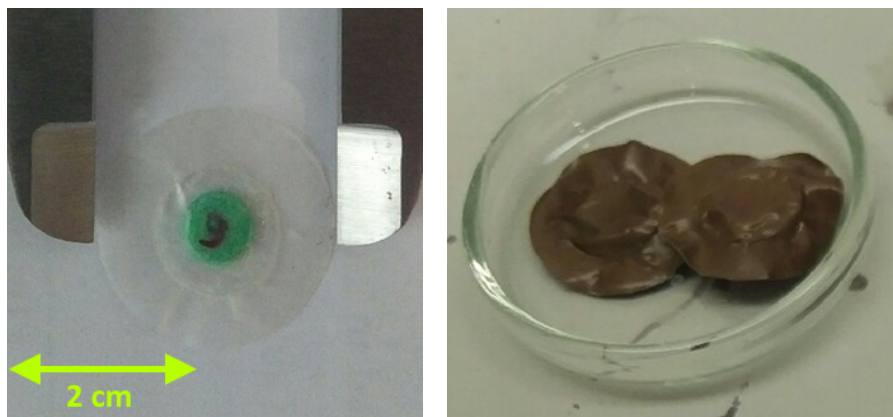
Figure 5
One of the prepared samples before the activation experimens (left) and after the reactor acti-
vation, showing color change as a result of radiation damage (right).

obstructed. The beam intensity during the ir-
radiation period was monitored by a Cividec
B6C neutron-sensitive diamond detector. The
activities of the reaction products [54]Mn and
[60]Co were quantified by high-resolution gam-
ma-ray spectrometry using a HPGe detector
and were in the order of 150-200 Bq for [54]Mn
and 30-40 Bq for ^{60}Co per sample, respec-
tively.

The second activation of the prepared sam-
ples was performed in the LVR-15 reactor at
ÚJV Řež, Czech Republic. A second activation
of the same samples was possible since the
high neutron flux inside a nuclear reactor
enables production of much higher quantities
of the activation products, compared to the
the cold neutron activation. The LVR-15 is a
light-water research reactor with a maximum
thermal power of 10 MW and maximum thermal
neutron flux of 10^{14} cm^{-2} s^{-1}. The samples were
irradiated inside an aluminum capsule at the
position „DONA 6" in the outer region of the

reactor core to assure a well-moderated neu-
tron spectrum[38]. The cadmium ratio method
was utilized to deduce the contribution of
epithermal neutrons to the observed activa-
tion. Two of the samples were irradiated bare
for 25 min, the final third sample was irradiated
in a cylindrical Cd case of 1 mm wall thickness
for a longer period of 3 hours. The neutron flux
and the spectrum were measured by co-acti-
vated metal foil as fluence monitors. The
post-irradiation activity quantification by gam-
ma-ray spectrometry was performed in iden-
tical manner as after the cold neutron activa-
tion. This time, activities of about 9000 Bq
[54]Mn and 2000 Bq ^{60}Co were produced in the
samples activated bare and 400 Bq [54]Mn and
300 Bq ^{60}Co in the Cd shielded sample.

The actual quantity measured in such ex-
periments is not the neutron capture
cross-section of [53]Mn itself, but the ratio of
this cross-section and the cross-section of the
monitor reaction [59]Co(n,γ). This cross-section

	σ_0 [barn]	I_0 [barn]
Cold neutron activation (this work)	75.44±0.94	–
Reactor activation (this work)	77.5±1.0	43.1±1.2
Average (this work)	76.5±1.4	43.1±1.2
Millard Jr. (1965)[28]	95±29	–
Honda (1971)[39]	82±7	–
Wölfle (1972)[30]	66±7	‹125
Mughabghab (6th Ed.)[27]	70±10	30±5 ?

Table 1
The neutron capture cross-section of ^{53}Mn for 2200 m/s neutrons σ_0 and the resonance integral I_0 obtained from the activation experiments with cold and reactor neutrons.

ratio remains basically constant over the whole 1/v range. Therefore, the thermal neutron capture cross-section σ_0 of ^{53}Mn (for 2200 m/s neutrons) can be calculated by multiplication of this ratio with the corresponding value of the „standard" thermal neutron capture cross-section of ^{59}Co, regardless of the actual experimental neutron energy (as long as there are no reconances close to the used energy range). Table 1 summarizes the thermal neutron capture cross-sections obtained from the activation experiments with cold and reactor neutrons and compares them to previously reported values. The two values of thermal capture cross-section obtained in our measurements match well to each other as well as to the older values and their average given by Mughabhab[27].

The final uncertainty is, however, one order of magnitude lower and with ~1.5 % similar to cross-section uncertainties of stable isotopes.

Besides the thermal neutron capture cross-section, the resonance integral I_0 of ^{53}Mn was measured during the reactor neutron activation as well. The reported value of 43.1 barn is, however, strictly valid only for the experimental reactor spectrum. Recalculation to the typically tabulated value for an ideal 1/E epithermal spectrum could not be performed due to the lack of data about the resonance structure of ^{53}Mn. Nevertheless, the correction is expected to be rather small, in the order of few percent and, thus, within the reported uncertainty of our value. This is the first ever measurement of the resonance integral of ^{53}Mn; although Mughabghab gives a value of 30±5 barn, this cannot be found in the referenced primary publications.

3.2 Capture cross-section at stellar neutron energies

Most of the stable isotopes beyond iron are produced in late stages of massive star evolution by consecutive neutron capture with subsequent β-decay – a process called slow neutron capture or s-process. The main neutron source for the s-process is the α-particle induced neutron emission in the ^{22}Ne(α,n) reaction. This thermonuclear reaction between helium and neon produces sufficient neutrons when the temperature T of the stellar environment reaches about 350 MK (million Kelvin) or, equivalently, kT = 30 keV when multiplied with the Planck constant.

Thus the most common used neutron-capture cross-section in astrophysical calculations is the 30keV Maxwellian-Averaged Cross-Section (MACS) which corresponds to a cross-section integrated over a Maxwellian neutron spectrum with kT = 30 keV. The MACS can be calculated, if the energy dependence of the cross-section over the relevant energy range (0-200 keV) is well known. For the mentioned case of s-process calculations, an uncertainty of the MACS below 5 % is desired in general[40]. This is particularly challenging as this energy interval overlaps the resolved resonance range of most nuclei, characterized by large spikes in the neutron cross-section. Hence, calculation of the MACS with high precision requires good knowledge of all resonance parameters in this energy range. For many stable and in particular radioactive nuclei, such as ^{53}Mn, the resonance parameters are not known at all and the excitation function can only be predicted theoretically based on
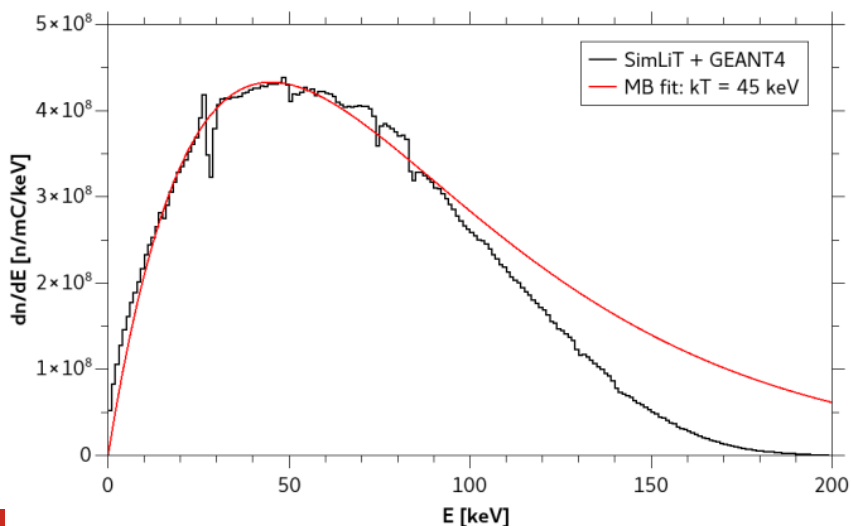

Figure 6

Neutron spectrum at sample position calculated by the SimLiT code[43] and the theoretical Maxwellian distribution with kT = 45 keV, providing the best fit of the data.

general phenomenological trends across the chart of the nuclei. Nevertheless, such predictions (as can be found in the TENDL library[31,32], presented in Fig. 4 for [53]Mn) still suffer from much higher systematic uncertainty than needed for astrophysical applications.

An option to directly asses the MACS experimentally, without the knowledge of the differential cross-section shape, is a cross-section measurement using a so-called "quasi-Maxwellian" neutron spectrum, i.e., a neutron spectrum very similar to the Maxwellian energy distribution. In experimetnal setups, the [7]Li(p,n) reaction (with a proton energy threshold of 1881 keV in the laboratory system) is typically exploited, yielding neutrons with a quasi-Maxwellian distributions in the kT-energy range from 15 keV to 50 keV, depending on the proton energy offset above the reaction threshold. The Liquid-Lithum Target (LiLiT)[41] of the SARAF facility at the Soreq NRC (Israel) was designed to produce an intense neutron field with such a quasi-Maxwellian energy distributions by bombarding a liquid lithium jet with a proton beam of up to 2 mA. The LiLiT setup was used for several measurements of MACSs at astrophysically relevant energies (see review[42] and the references therein).

A sample containing ~10^{18} atoms [53]Mn was prepared and characterized in similar manner like in the previously described activation experiments with cold and thermal neutrons. The diameter of the filter disc was, however, increased to 20 mm to maximize the beam interception as the neutrons are emitted in a forward-directed cone. Kapton tape was used to seal the filter disc. The sample was put into an aluminum case with front wall thickness of 0.5 mm. Gold foils mounted externally on

the case were used as neutron fluence monitors. Although the neutron spectrum ressembles almost perfectly a Maxwellian distribution with kT = 30 keV at a proton energy of about 1920 keV, the neutron yield increases significantly for higher proton energies. The neutron spectrum from the here used energy of 1946 keV can be adequately fitted as a Maxwellian neutron distribution with kT = 45 keV (see Fig. 6), but has an enhancement of the neutron flux by a factor of two to three. An activity of about 1 Bq [54]Mn was produced during 4 days of irradiation with accumulated proton dose on LiLiT target of 22.3 mAh. The variations of the beam intensity with time were recorded using a dose rate meter positioned in the target room.

The produced amounts of [54]Mn were quantified by high-resolution gamma-ray spectrometry at PSI, Soreq NRC and Hebrew University in Jerusalem (Israel). The measured value can be transformed into a 30 keV MACS of about 40 mbarn which is significantly lower than all theoretical predictions, varying between 100-200 mbarn in the different versions of the TENDL-library.

4. Half-life measurement of [53]Mn

[53]Mn decays by electron capture (EC) with a half-life of about 3.7 Ma to the stable chromium isotope [53]Cr. Half-lives of this order of magnitude cannot be measured directly by simply following the radioactive decay. Instead, the following basic relation must be utilized:

$$t_{1/2} = \ln(2) \cdot \frac{N}{A}$$

where N and A denote the concentration and specific activity of the radionuclide within a
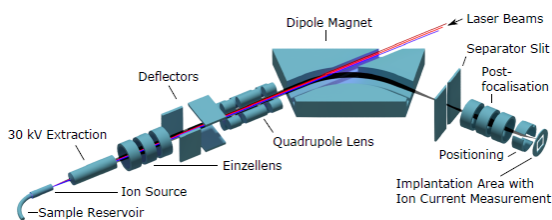
Figure 7
The RISIKO mass separator[44] (left); One of the three 6μm Al foils with implanted [53]Mn. The implantation area is visible as a darker spot of about 12 mm diameter in the middle of the foil (right).

sample, respectively, and $t_{1/2}$ the sought half-life. The decay of [53]Mn is not accompanied by any emission of gamma-rays, only low-energy relaxation radiation (electrons and X-rays) is emitted during the re-arrangement of the electronic shells after the decay to the daughter nuclide [53]Cr. Liquid scintillation (LS) counting is the method of choice for activity determination of low and medium Z pure EC-decay radionuclides like [53]Mn due to its relatively high detection efficiency compared with other methods. The sample used for LS measurements has to be of high radiochemical purity because of the limited spectroscopical capabilities of LS. As discussed above the [53]Mn material available at PSI was extracted from highly-activated accelerator waste. Whereas other radiochemical impurities could be removed from the [53]Mn fraction by chemical methods, a non-negligible amount of [54]Mn remained since isotopes of the same element behave identically during chemical treatment. Thus, mass separation by laser resonance-ionization mass-spectroscopy (RIMS) was performed using the RISIKO separator at the University Mainz (see Fig. 7) to obtain a iso-topically pure [53]Mn sample. A novel three-step ionization scheme was developed, enabling separation and implantation of manganese with an overall efficiency of up to 30 %[44]. Even at a high implantation current of 100 nA, necessary to process the required amounts of [53]Mn, efficiencies between 10 and 20 % could be maintained. During a three week campaign a total of 1.2 kBq (or 2×10^{17} atoms) [53]Mn was mass separated and implanted into three 6 μm thick Al foils (an example is shown in Fig. 7). This amount is conveniently measurable by LS counting, even when split into several individual samples.

The central parts of the foils with implanted [53]Mn were punched out, dissolved and transferred to 0.1 M HCl. The majority of this stock solution was shipped to PTB (Physikalisch-Technische Bundesanstalt), Braunschweig (Germany), in a crimped glass vial. The determination of the [53]Mn concentration was performed by ICP-MS at PSI HotLab facility, in an analogous manner to the analyses described in the frame of the cross-section measure-

ments. The specific activity measurements were carried out using the TDCR (triple-to-double-coincidence ratio) method[45] with a total of five LS ounters at the national metrological institutes PTB, Braunschweig (Germany) and LNHB, Saclay (France). Preliminary studies were performed at PSI to confirm the compatibility as well as the long-term stability of model solutions of similar chemical composition as the ^{53}Mn stock solution with the used Ultima Gold scintillator cocktail. The analysis of the experimental data were carried out with state-of-the-art methods using a stochastic model for the atomic rearrangement and taking into account all required corrections[46]. Supplementary measurements were performed using commercial LS counters. The obtained LS spectra confirm the absence of any radioactive impurity. The activity determination requires some nuclear decay data as input for the efficiency computation. In particular the fractional electron-capture probabilities of the 2nd forbidden non-unique transition are needed. Improved theoretical calculations which take all required corrections and the atomic and nuclear structure into account are still ongoing[47]. Hence, the activity determination and the related uncertainty estimation are still in progress. The preliminary results suggest a half-life value of approx. 3.4 Ma years, i.e., slightly lower than the older value, but compatible within one standard uncertainty. Similarly to the cross-section, however, the uncertainty of this value is dramatically reduced, from 10 % to about 1 %.

5. Conclusions & Outlook

In the frame of this project, the half-life of the short-lived cosmogenic radionuclide ^{53}Mn and its neutron capture cross-section at different neutron energies were measured. These experiments used the worldwide-unique stock of ^{53}Mn, which was obtained from accelerator waste at PSI in the frame of the ERAWAST project. The newly obtained value of the decay half-life (which is yet to be finalized in following months) and the thermal neutron capture cross-sections show good agreement with older values. The uncertainty of these values, however, could be improved by our work by an order of magnitude to a level of 1-2 %, a precision level fulfilling the requirements of the application of ^{53}Mn in geological dating both in space and on Earth. Additionally, thanks to employing ICP-MS as a method for the determination of the ^{53}Mn concentration in our experiments instead of activity measurements, the thermal cross-section value of ^{53}Mn is not dependent on the ^{53}Mn half-life value (or vice versa), in contrast to the majority of the older experiments.

Furthermore, the resonance integral and the 30 keV MACS of the reaction ^{53}Mn(n,γ) were measured for the first time. These cross-section values can be utilized directly for reactor NAA and for astrophysical calculations, respectively. Additionally, they provide valuable hints about the resolved resonance range of ^{53}Mn which can be used for further improvement of cross-section predictions in the TENDL library or similar projects. Corresponding works have been initiated already. Both the resonance integral and the 30 keV MACS are surprisingly low, compared to the

considerably high thermal neutron capture cross-section. A possible explanation to this factcould be the presence of a neutron resonance in the vicinity of the thermal region. To further investigate this possibility, a cross-section measurement with very cold neutrons at the PF2 beamline of ILL was initiated. The activation experiment was successfully performed at ILL, but the analysis of the data is still ongoing.

The works performed in the frame of this Ph.D. thesis will lead to several publications in scientific journals. The results of the thermal cross-section measurement with cold and reactor neutrons has been already published in PRC[48,] an article dealing with the cross-section determination at stellar neutron energies has been submitted to PRL[49] and is currently under revision. Manuscripts of additional publications, describing the novel method of cross-section measurement with UCNs, the mass separation of kBq amounts of ^{53}Mn using laser ionization mass spectroscopy and the half-life determination of ^{53}Mn are in preparation for publication in 2021. Finally an article will present the cross-section measurement with VCNs.

Acknowledgements

REFERENCES

[1] F.-K. Thielemann, K. Nomoto, M.-A. Hashimoto, Astrophys. J. **460**, 408 (1996), https://doi.org/10.1086/176980

[2] K. Maeda, et al., Astrophys. J. **712**, 624 (2010), https://doi.org/10.1088/0004-637x/712/1/624

[3] N. E. Yanasak, et al., Astrophys. J. **563**, 768 (2001), https://doi.org/10.1086/323842

[4] D. Koll, et al., Phys. Rev. Lett. **123**, 072701 (2019), https://doi.org/10.1103/physrevlett.123.072701

[5] J. Feige, et al., Publ. Astron. Soc. Aust. **29**, 109 (2012), https://doi.org/10.1071/as11070

[6] J. Feige, et al., EPJ Web of Conferences **63**, 03003 (2013), https://doi.org/10.1051/epjconf/20136303003

[7] B. J. Fry, B. D. Fields, J. R. Ellis, Astrophys. J. **800**, 71 (2015), https://doi.org/10.1088/0004-637x/800/1/71

[8] B. W. Grefenstette, et al., Astrophys J. **834**, 19 (2016), https://doi.org/10.3847/1538-4357/834/1/19

[9] G. Lugmair, A. Shukolyukov, Geochim. Cosmochim. Acta **62**, 2863 (1998), https://doi.org/10.1016/s0016-7037(98)00189-6

[10] M. Lugaro, et al., Meteorit. Planet. Sci. **47**, 1998 (2012), https://doi.org/10.1111/j.1945-5100.2012.01411.x

[11] J. Schaeffer, et al., Earth Planet. Sci. Lett. **251**, 334 (2006), https://doi.org/10.1016/j.epsl.2006.09.016

[12] M. Imamura, R. Finkel, M. Wahlen, Earth Planet. Sci. Lett. **20**, 107 (1973), https://doi.org/10.1016/0012-821x(73)90146-5

[13] M. Poutivtsev, et al., NIM B **268**, 756 (2010), https://doi.org/10.1016/j.nimb.2009.10.023

[14] D. Schumann, J. Neuhausen, J. Phys. G **35**, 014046 (2007), https://doi.org/10.1088/0954-3899/35/1/014046

[15] M. Barbagallo, et al., Phys. Rev. Lett. **117**, 152701 (2016), https://doi.org/10.1103/physrevlett.117.152701

[16] E. Maugeri, et al., J. Instrum. **12**, P02016 (2017), https://doi.org/10.1088/1748-0221/12/02/p02016

[17] L. Damone, et al., Phys. Rev. Lett. **121**, 042701 (2018), https://doi.org/10.1103/physrevlett.121.042701

[18] E. Maugeri, et al., NIM A **889**, 138 (2018), https://doi.org/10.1016/j.nima.2018.01.078

[19] S. Heinitz, et al., Appl. Radiat. Isot. **130**, 260 (2017), https://doi.org/10.1016/j.apradiso.2017.10.012

[20] T. Al-Abdullah, et al., Eur. Phys. J. A **50**, 140 (2014), https://doi.org/10.1140/epja/i2014-14140-8

[21] V. Margerin, Phys. Lett. B **731**, 358 (2014), https://doi.org/10.1016/j.physletb.2014.03.003

[22] G. Rugel, et al., Phys. Rev. Lett. **103**, 072502 (2009), https://doi.org/10.1103/physrevlett.103.072502

[23] A. Wallner, et al., Phys. Rev. Lett. **114**, 041101 (2015), https://doi.org/10.1103/physrevlett.114.041101

[24] D. Schumann, N. Kivel, R. Dressler, PLOS ONE **14**, e0219039 (2019), https://doi.org/10.1371/journal.pone.0219039

[25] D. Schumann, et al., Radiochim. Acta **97**, 123 (2009), https://doi.org/10.1524/ract.2009.1585

[26] M. Ayranov, D. Schumann, J. Radioanal. Nucl. Chemi. **286**, 649 (2010), https://doi.org/10.1007/s10967-010-0732-0

[27] S. F. Mughabghab (ed.), Atlas of Neutron Resonances, 6th Edition (Elsevier, 2018)

[28] H. T. Millard, Science **147**, 503 (1965), https://doi.org/10.1126/science.147.3657.503

[29] M. Imamura, et. al., Earth Planet. Sci. Lett. **6**, 165 (1969), https://doi.org/10.1016/0012-821x(69)90085-5

[30] R. Wölfle, Radiochim. Acta **18**, 207 (1972), https://doi.org/10.1524/ract.1972.18.4.207

[31] A. Koning, D. Rochman, Nucl. Data Sheets **113**, 2841 (2012), https://doi.org/10.1016/j.nds.2012.11.002

[32] A. Koning, et al., Nucl. Data Sheets **155**, 1 (2019), https://doi.org/10.1016/j.nds.2019.01.002

[33] O. Reinitz, Tagungsbericht 4. VDI Fachtagung Messunsicherheit praxisgerecht bestimmen, 12-13. November 2008, Erfurt (Germany)

[34] A.-L. Hauswirth, et al., Accred. Qual. Assur. **17**, 129 (2011), https://doi.org/10.1007/s00769-011-0827-5

[35] J. Vogl, W. Pritzkow, MAPAN **25**, 135 (2010), https://doi.org/10.1007/s12647-010-0017-7

[36] J. Fonslet, Appl. Radiat. Isot. **121**, 38 (2017), https://doi.org/10.1016/j.apradiso.2016.11.021

[37] A. Kaestner, et al., NIM A **659**, 387 (2011), https://doi.org/10.1016/j.nima.2011.08.022

[38] M. Koleška, et al., J. Radioanal. Nucl. Chem. **305**, 51 (2015), https://doi.org/10.1007/s10967-015-4025-5

[39] M. Honda, M. Imamura, Phys. Rev. C **4**, 1182 (1971), https://doi.org/10.1103/physrevc.4.1182

[40] M. Wiescher, F. Käppeler, K. Langanke, Annu. Rev. Astron. Astrophys. **50**, 165 (2012), https://doi.org/10.1146/annurev-astro-081811-125543

[41] S. Halfon, et al., Rev. Sci Instrum. **84**, 123507 (2013), https://doi.org/10.1063/1.4847158

[42] M. Paul, et al., Eur. Phys. J. A **55**, 44 (2019), https://doi.org/10.1140/epja/i2019-12723-5

[43] M. Friedman, et al., NIM A **698**, 117 (2013), https://doi.org/10.1016/j.nima.2012.09.027

[44] N. Kneip, Master's Thesis, JGU Mainz, Germany (2018)

[45] R. Broda, P. Cassette, K. Kossert, Metrologia **44**, S36 (2007), https://doi.org/10.1088/0026-1394/44/4/s06

[46] K. Kossert, A. G. Carles, Appl. Radiat. Isot. **68**, 1482 (2010), https://doi.org/10.1016/j.apradiso.2009.11.048

[47] X. Mougeot, Appl. Radiat. Isot. **154**, 108884 (2019), https://doi.org/10.1016/j.apradiso.2019.108884

[48] J. Ulrich, et al., Phys. Rev. C **102**, 024613 (2020), https://doi.org/10.1103/PhysRevC.102.024613

[49] J. Ulrich, et al., Phys. Rev. Lett., submitted (2020)

Minutes of the SNSS/SGN General Assembly 2020

Date/Location
October 29, 2020, Zoom meeting

Start
14:00

End
17:00

Participants
29 members of the society
6 non-members

1. Welcome

Henrik Ronnow, president of the Swiss Neutron Science Society, welcomes the participants to the general assembly 2020.

The assembly was preceded by 2 scientific presentations by the two winners of the 2020 Young Scientist Prize of the SNSS sponsored by SwissNeutronics.

2. Minutes of the General Assembly 2019

The minutes of the general assembly of the SNSS/SGN from 22.11.2019, published in Swiss Neutron News #55 are accepted without objections.

3. Annual Report of the Chairman

H. Ronnow reports on the activities of the SNSS/SGN in the years 2019 and 2020:

a. The seventh (2020) **Young Scientist Prize** of the SNSS/SGN sponsored by Swiss Neutronics has been split and was awarded to Dr. Muriel Siegwart and Dr. Jiri Ulrich.

b. One issue of **Swiss Neutron News** has appeared in April 2020 and another issue will be distributed in November 2020.

c. The SNSS/SGN has **203 members** at the time of the assembly. The number of mem-

bers has increased by 17 in one year. However, the number of SNSS members is still significantly lower than that of neutron users in Switzerland. The visibility of the SNSS should be improved for all neutron users, especially new users.

d. The Swiss membership of the ILL and the ESS has been secured for the years 2020 - 2024 with new contracts.

e. The SNSS is invited to meetings with the Swiss Academy of Sciences (SCNAT) and the State Secretariat for Education, Research, and Innovation (SERI) to plan the development of research in Switzerland and the Swiss participation in large facilities such as the ILL and the ESS. For the next dispatch of SERI to the Federal Council for the years 2025-2028, the SNSS is working on a **Swiss Neutron Roadmap**. A first draft of this road-map is planned to be available end of December 2020. The final version is planned for end of March 2021.

4. Report of the Treasurer

The annual balance sheet for 2019 is presented:
Assets SNSS/SGN on 1.1.2019: **CHF 6867.15**

	Revenues [CHF]	Expenses [CHF]
Membership-fees (cash box)	80.00	
Membership-fees (postal check acc.)	590.00	
Donations	10.00	
Deposit prize money 2019	1000.00	
Deposit prize money (cash box)	1000.00	
Expenses Postfinance account		63.85
Refund wrong transfer		180.00
Payout prize money 2019		1000.00
Total	2680.00	1243.85
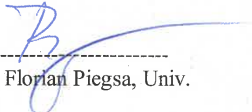
Net earnings 2019	**CHF 1436.15**	

Balance sheet 2019:	Assets [CHF]	Liabilities [CHF]
Postfinance account	8147.15	
Cash box	156.15	
Assets on 31.12.2019	**8303.30**	

5. Report of the Auditors

Bericht der Revisoren

Die Rechnungsrevisoren haben die Belege, die Abrechnungen und die Bilanz für das Jahr 2019 geprüft und für in Ordnung befunden!

17.1.2020	M. Zolliker	29.1.2020	B
Datum	Dr. M. Zolliker, PSI	Datum	Prof. Florian Piegsa, Univ. Bern

Both Auditors (M. Zolliker and F. Piegsa) have examined the bookkeeping and the balance sheet for 2019. They have accepted it without objection. The participants unanimously vote for the release of the SGN/SNSS board.

6. Budget 2020

H. Ronnow presents the following proposal for the budget 2021:

	Receipts [CHF]	Expenditures [CHF]
member fees	700.00	
interest	0.00	
prize money	1000.00	1000.00
fees PC account		63.00
Total	1700.00	1063.00
Total receipts 2020	637.00	
Assets 31.12.2020	8940.30	

The participants accept the budget proposal without objection.

H. Ronnow mentions that the SNSS could join the Swiss Academy of Sciences (scnat). The annual membership costs would be CHF 7.00 per member of the SNSS, but the SNSS might be able to receive more money than the membership fee. The SNSS board will look into the possibilities to join scnat under acceptable conditions and will report at the general assembly in 2021.

7. Revised SNSS Statutes

As the name of the society was changed from "Swiss Neutron Scattering Society" to "Swiss Neutron Science Society", the statutes have to be updated. The new statutes are presented with highlighted changes, and the updated statutes are accepted unanimously.

8. News from SINQ (M. Kenzelmann)

a. The important milestones of the 2019/2020 SINQ-upgrade have been met in spite of the Corona pandemic. SINQ resumed operation in July 2020 with only a small delay of 2 months caused by the pandemic. First measurements have shown that the instrument-dependent flux increase is in the expected range of a factor 2 to 10.

b. Due to the upgrade, there was only one call for proposals in 2019 and the number of received proposals was high. The user program on the commissioned instruments was, however, strongly affected by the travel restrictions due to the Corona pandemic. Experiments were carried out with mailed-in samples when possible, but a significant number of experiments had to be postponed to 2021.

c. The term of Prof. Peter Boeni as chair of the Strategic Advisory Committee (SAC) of SINQ has ended in 2019. Prof. Stefan Klotz has been a SAC member since 2013 and has accepted to be the new chair.

d. Several instrumentation projects at SINQ are being continued in 2021. The SANS instrument PA20 is transferred to PSI from the Laboratoire Léon Brillouin (Saclay, France) and is planned to be commissioned in spring 2022. The Laue diffractometer Falcon from the Helmholtz Zentrum Berlin will be installed at SINQ with a new front end developed at PSI.

e. The decommissioned instrument SANS-II will be transferred to Argentina and a collaboration of PSI and Argentina for the support of sample environments and software for neutron instruments will be started.

9. News from ENSA, ILL, and ESS (H. Ronnow)

I) News from ILL

a. The 2019-2023 contract for the Swiss participation in the ILL has been signed by the State Secretariat for Education, Research and Innovation (SERI). The annual funding is secured until 2028 in the SERI Botschaft but was reduced from 15 MCHF to 12 MCHF.

b. In addition to the annual funding for the ILL, a budget for supplementary measures has been approved by SERI. Projects for the ILL that are carried out in Switzerland can be financed via the budget of the supplementary measures.

c. The Swiss participation in the CRG instruments IN12, IN22, and D23 operated by CEA helps to reduce the number of Swiss beamtime proposals being rejected due to national balance. Swiss users obtain beam time on these CRG instruments via the normal proposal system of the ILL. The Swiss participation in these CRG instruments has been extended to 2022 and may be continued further.

d. In case your proposal is impeded by national balance, please send a short notice to the SNSS (sgn@psi.ch) to make sure that the SNSS can document the effect of the national balance.

e. Some countries are arrears with their pay-

ments to the ILL. Proposals with co-proposers from these countries have, therefore, not received beam time.

f. In 2019 and 2020, the ILL reactor was in operation for only two cycles per year (about 100 days per year). Three reactor cycles with a total of about 176 beam days are planned for 2021.

II) News from ESS

a. Since 2019, important steps towards the completion of ESS have been made. ESS is now about 73% complete and user operation is planned to start in 2023. Sweden was not slowed down as much as other countries by the COVID pandemic, and the construction of ESS did profit from this.

b. The overall ESS construction budget is tight. The budget contributions for the future operation of ESS are still being negotiated.

c. Switzerland is a strong contributor to the ESS and is involved in five instruments for ESS: ESTIA, BIFROST, HEIMDAL, ODIN, and MAGIC. The reflectometer ESTIA (100% Swiss) is planned to be among the first instruments.

III) News from ENSA

a. On Nov. 28 2019, Henrik Ronnow, president of SNSS, has been elected new chair of ENSA. Lambert van Eijck was elected vice chair and Natalie Malikova has become the new secretary of ENSA.

b. Henrik Ronnow plans to give up the SNSS presidency in 2021. A new president must be elected at the 2021 General Assembly. Candidates or suggestions for the next president are most welcome.

c. The ICNS 2021 will be held in Buenos Aires, Argentina, and the ECNS 2023 will take place in Munich, Germany. After two unsuccessful applications, this was the third application of Munich for an ECNS conference. The proposal of PSI and SNSS for the ECNS 2023 in Basel, Switzerland, was rejected.

d. ENSA is a partner of the accepted European funding proposal BrightnESS2, a European-Union funded project to support the long-term sustainability of ESS, its community, and the network of neutron sources in Europe. In particular, the European user community will be analyzed and access models for ESS will be explored.

10. Miscellaneous

No further issues are discussed.

U. Gasser
December 2020

Announcements

SGN/SNSS Members

Presently the SGN/SNSS has 203 members. New members can register online on the SGN/SNSS website: http://sgn.web.psi.ch

SGN/SNSS Annual Member Fee

The SGN/SNSS members are kindly asked to pay their annual member fees. At the general assembly 2013 of the society, the fee has been increased from CHF 10 to **CHF 20**. It can be paid either by bank transfer or in cash during your next visit at PSI. The bank account of the society is accessible for both Swiss national and international bank transfers:
Postfinance: 50-70723-6 (BIC: POFICHBE), IBAN: CH39 0900 0000 5007 0723 6.

The SGN/SNSS is an organisation with tax charitable status. All fees and donations payed to the SGN/SNSS are **tax deductible**.

PSI Facility News

Recent news and scientific highlights of the three major PSI user facilities SLS, SINQ and SµS can be found in the **quarterly electronic newsletter** available online under:
https://www.psi.ch/science/facility-newsletter

SINQ Upgrade

In 2020, SINQ was put back into operation in mid July with only a small delay because of the Corona pandemic. The first measurements on the instruments SANS-I, TASP, FOCUS, MORPHEUS, NARZISS, and ORION with upgraded guides did show that the expected flux gains have been reached. The spectrometer CAMEA joined the user operation in the second half of the user cycle in 2020.

The diffractometer DMC receives a new ^{3}He detector and commissioning is planned for the second user cycle of 2021. The second instrument with a complete redesign is the reflectometer AMOR. It has received the new

fully focusing Selene optics. Commissioning is planned for 2022.

Many experiments in the user cycle of 2020 were affected by travel restrictions due to the quickly evolving Corona situation. A good number of experiments could be carried out with mailed-in samples in the absence of the neutron users, while other experiments had to be postponed to 2021.

Two user cycles are planned for 2021. As the Corona situation continues to evolve and severe travel restrictions still apply, the first user cycle of 2021 will also be affected by the pandemic. Beam-time proposals that can be carried out in the absence of the users, can be scheduled at the beginning of the first user cycle.

Please visit the page https://www.psi.ch/sinq/call-for-proposals to obtain the latest information about beam cycles and the availability of the neutron instruments.

Registration of publications

Please remember to **register all publications either based on data taken at SINQ, SLS, SµS or having a PSI co-author** to the Digital Object Repository at PSI (DORA):
www.dora.lib4ri.ch/psi/
Please follow the link 'Add Publication'.

Open Positions at SINQ and ILL

To look for open positions at SINQ or ILL, have a look at the following webpages:
https://www.psi.ch/pa/stellenangebote
https://www.ill.eu/careers/all-our-vacancies/?L=0

PhD positions at ILL

The PhD program of the Institut Laue-Langevin, ILL, is open to researchers in Switzerland. Consult the page https://www.ill.eu/careers/all-our-vacancies/phd-recruitment for information on the PhD program of ILL or get in contact with the managers of the program using the email address phd@ill.fr.

The Swiss agreement with the ILL includes that ILL funds and hosts one PhD student from Switzerland.

Conferences and Workshops 2021 and beyond

An updated list with online links can be found here: http://www.psi.ch/useroffice/conference-calendar

May 2021

SupraBio 2021, International Symposium on SupraBiomolecular Systems
May 10-12, 2021, online

Swedish Neutron Week 2021
May 10-12, 2021, online

10th International Conference of the Hellenic Crystallographic Association
May 14-16, 2021, Athens, Greece

QENS/WINS 2021
May 17-21, 2021, online

Neutron Scattering in Colloid and Interface Science
May 18 and 25, 2021, online

RI Logistics - Getting Science in Place
May 19-20, 2021, online

EMBO workshop on Molecular Neurobiology
May 21-25, 2021, Heraklion, Crete, Greece

SIAM Conference on Mathematical Aspects of Materials Science
May 24-29, 2021, Bilbao, Spain

Magnetic Small Angle Neutron Scattering – from Nanoscale Magnetism to Long-Range Magnetic Structures
May 30-3 June, hybrid seminar, Tutzing, Germany

June 2021

International Conference on Research Infrastructures (ICRI)
June 1-3, 2021, online

2021 Annual MLZ Conference: Neutrons for Life Sciences
June 8-11, 2021, online

2nd COMPPÅ Symposium on Membrane Protein Production and Analysis
June 9-11, 2021, New York, USA

SXNS16: 16th International Conference on Surface X-ray and Neutron Scattering
June 14-18, 2021, Lund, Sweden

EPDIC17 - The European Powder Diffraction Conference
June 15-18, 2021, Sibenik, Croatia

PSI Master School 2021
June 21-25, 2021, Villigen, Switzerland

ACS meeting: 37th National Medicinal Chemistry Symposium
June 27-30, 2021, New York, NY, USA

AFC 2020: Congress of the French Association of Crystallography
June 29 - July 2, 2021, Grenoble, France

July 2021

ICNS 2021: International Conference on Neutron Scattering 2021
July 4-8, 2021, Argentina

15th International Conference on Muon Spin Rotation, Relaxation and Resonance
July 4-9, 2021, Parma, Italy

ECS 6: Sixth European Crystallographic School
July 4-10, 2021, Budapest, Hungary

23rd National School on Neutron and X-Ray Scattering
July 12-30, 2021, online

August 2021

IUCr2020 Computing School
August 9-14, 2021, Nove Hrady, Czech Republic

School on SAXS/SANS and BioSAXS/BioSANS data analysis
August 11-13, 2021, Kutná Hora, Prague, Czech Republic

Electron Crystallography School - 3D Electron Diffraction/MicroED Bridging Small Molecule and Macromolecular Crystallography
August 11-14, 2021, Tabor, Czech Republic

TOPAS Intensive Course
August 12-14, 2021, Prague, Czech Republic

25th General Assembly and Congress of the International Union of Crystallography (IUCr)
August 14-22, 2021, Prague, Czech Republic

PSI Condensed Matter Camp
August 16-20, 2021, Zuoz, Switzerland

ECM33: 33rd European Crystallographic Meeting
August 24-28, 2021, Versailles, France

RIXS-REXS 2020: Workshop on Resonant Elastic and Inelastic X-ray Scattering 2020
August 25-27, 2021, Port Jefferson, NY, USA

JCNS Laboratory Course 2021
August 30 - September 10, 2021, Jülich and Garching, Germany

September 2021

9th International Conference on Electron Tomography
September 12-15, 2021, Egmond aan Zee, The Netherlands

MUST2021: The International Conference on Molecular Ultrafast Science and Technology
September 12-16, 2021, Grindelwald, Switzerland

XTOP2020: 15th Biennial Conference on High-Resolution X-Ray Diffraction and Imaging
September 12-17, 2021, Minsk, Belarus

COHERENCE 2021: International Conference on Phase Retrieval and Coherent Scattering
September 13-16, 2021, Shanghai, China

Big Science Business Forum 2021
September 28 - October 1, 2021, Granada, Spain

October 2021

SMS 2021: Smart Materials and Surfaces
October 20-22, 2021, Milan, Italy

The 6th Edition of the Europe Graphene Forum EGF 2021
October 20-22, 2021, Milan, Italy

School of Solid State Physics: Dynamics of Electrons in Atomic and Molecular Nano-clusters
October 24-30, 2021, Erice, Italy

December 2021

Italian Crystal Growth - Crystal Growth: From Theory to Application
December 16-17, 2021, Torino, Italy

January 2022

Third Pan African Conference on Crystallo-graphy
January 17-22, 2022, Nairobi, Kenya

May 2022

LEAPS meets Quantum Technology Conference
May 16-20, 2022, Erice, Italy

QENS/WINS 2022
May 23-27, 2022, San Sebastian, Spain

September 2022

Diffusion Fundamentals IX
September 21-24, 2022, Krakow, Poland

Editorial

Join the Swiss Neutron Science Society...

to support all science using neutron radiation in Switzerland.
The Swiss Neutron Science Society is open to everybody interested in neutron scattering and research using neutron radiation in general.

The annual membership fee is CHF 20.-, but the membership is free for Bachelor-, Master-, and PhD-students.

Send an email to sgn@psi.ch to join.